

On the production of He, C, and N by low- and intermediate-mass stars: a comparison of observed and model-predicted planetary nebula abundances

R. B. C. Henry,^{1★} B. G. Stephenson,¹ M. M. Miller Bertolami,² K. B. Kwitter³ and B. Balick⁴

¹*Department of Physics and Astronomy, University of Oklahoma, Norman OK 73019, USA*

²*Instituto de Astrofísica de La Plata, UNLP-CONICET, Paseo del Bosque s/n, B1900FWA La Plata, Argentina*

³*Department of Astronomy, Williams College, Williamstown, MA 01267, USA*

⁴*Department of Astronomy, University of Washington, Seattle, WA 98195, USA*

Accepted 2017 August 31. Received 2017 July 28; in original form 2017 June 9

ABSTRACT

The primary goal of this paper is to make a direct comparison between the measured and model-predicted abundances of He, C, and N in a sample of 35 well-observed Galactic planetary nebulae (PNe). All observations, data reductions, and abundance determinations were performed in house to ensure maximum homogeneity. Progenitor star masses ($M \leq 4 M_{\odot}$) were inferred using two published sets of post-asymptotic giant branch model tracks and L and T_{eff} values. We conclude the following: (1) the mean values of N/O across the progenitor mass range exceeds the solar value, indicating significant N enrichment in the majority of our objects; (2) the onset of hot bottom burning appears to begin around $2 M_{\odot}$, i.e. lower than $\sim 5 M_{\odot}$ implied by theory; (3) most of our objects show a clear He enrichment, as expected from dredge-up episodes; (4) the average sample C/O value is 1.23, consistent with the effects of third dredge up; and (5) model grids used to compare to observations successfully span the distribution over metallicity space of all C/O and many He/H data points but mostly fail to do so in the case of N/O. The evident enrichment of N in PN and the general discrepancy between the observed and model-predicted N/O abundance ratios signal the need for extra mixing as an effect of rotation and/or thermohaline mixing in the models. The unexpectedly high N enrichment that is implied here for low-mass stars, if confirmed, will likely impact our conclusions about the source of N in the Universe.

Key words: stars: AGB and post-AGB – stars: evolution – ISM: abundances – planetary nebulae: general – galaxies: abundances – galaxies: ISM.

1 INTRODUCTION

Galaxies evolve chemically because hydrogen-rich interstellar material forms stars which subsequently convert a fraction of the hydrogen into heavier elements. These nuclear products are expelled into the interstellar medium (ISM) and thereby enrich it. As this cycle is continuously repeated, the mass fraction of metals rises. Additional factors which influence the metal abundances in galaxies include the exchange of gas with the intergalactic medium via inflow and outflow.

A crucial component for understanding the rate at which the interstellar abundance of a specific element rises over time is the amount

of the element that is synthesized and expelled by a star of a specific mass during its lifetime, i.e. the stellar yield. Generally, stellar yields are estimated by computing stellar evolution models that predict them. These models are constrained using elemental abundance measurements of the material that is cast off from the star in the form of winds propelled by radiation pressure, periodic expulsions by stellar pulsations, or sudden ejection caused by explosions.

In the current study, we are interested in the production of He, C, and N by low- and intermediate-mass stars (LIMS), that is, those stars typically considered to occupy the mass range of $1\text{--}8 M_{\odot}$. Stellar models suggest that internal temperatures become sufficiently high either in the cores or outer shells of these stars to drive not only the conversion of H to He via the proton–proton chain reactions, but also the triple alpha process as well as the CN(O) cycle to produce C and N, respectively. Observationally, there is

★ E-mail: rhenny@ou.edu

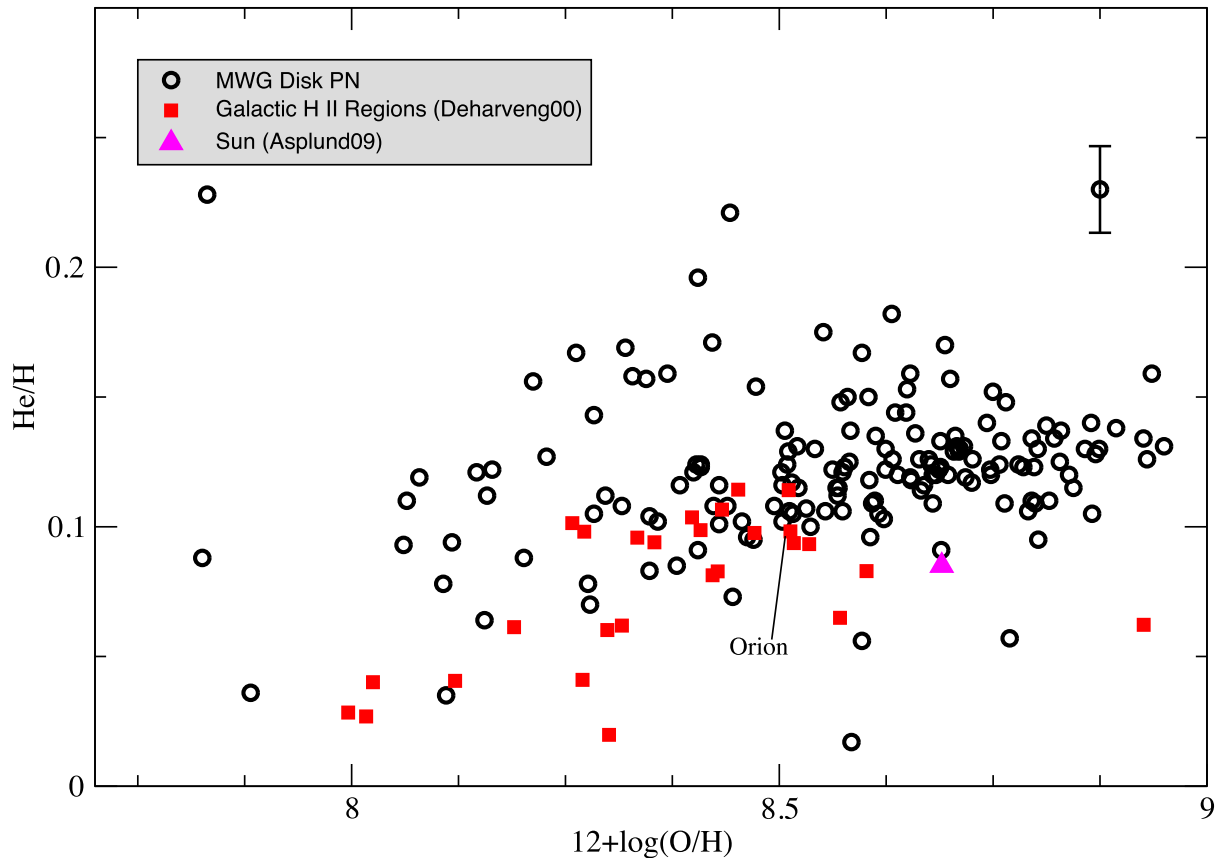


Figure 1. He/H versus $12+\log(\text{O}/\text{H})$. Open black circles refer to PN located in the MWG disc and taken from our extended sample, filled red squares represent Galactic H II regions from Deharveng et al. (2000), and the filled magenta triangle shows the solar position (Asplund et al. 2009). The position of Orion (Esteban et al. 2004) is indicated.

overwhelming evidence that LIMS do indeed synthesize and eventually expel measurable amounts of elements such as He, C, N, and perhaps O, as well as s-process elements (see articles by Herwig 2005; Kwitter & Henry 2012; Karakas & Lattanzio 2014; Delgado-Inglada 2016; Maciel, Costa & Cavichia 2017; Sterling 2017). However, the impact that LIMS actually have, relative to massive stars on the chemical evolution of these elements in a galaxy, is still very much open for debate.

The material that is cast off by LIMS during and after the asymptotic giant branch (AGB) stage in the form of winds of varying speeds can subsequently form large-scale density enhancements and become photoionized by the UV photons produced by the hot, shrinking stellar remnant, forming a planetary nebula (PN). The photon energy absorbed by the nebula results in the production of detectable emission lines that can be analysed in detail to infer abundance, temperature, and density information about the PN.

PN abundance patterns reflect the nature of the chemical composition of the LIMS atmospheres at the end of stellar evolution and are therefore useful in two ways. First, the abundances of alpha, Fe-peak, and r-process elements relative to H, especially O/H, Ne/H, S/H, Ar/H, and Cl/H in PN, evidently represent the levels of these elements that were present in the interstellar material out of which the progenitor star formed. This conclusion is strongly supported by a recent study by Maciel et al. (2017). This team has recently compiled and analysed a data base containing abundance measurements of 1318 PN along with a second data base containing similar information about 936 H II regions, the latter objects representing the current ISM abundance picture. Through the use of histograms

and scatter plots, the authors show that both object types exhibit the same lockstep behaviour of Ne/H, S/H, and Ar/H, all versus O/H.¹ This familiar result strongly supports the idea that LIMS do not themselves alter the levels of the alpha elements that were present in the interstellar material out of which they formed. As a result, PN can be used as probes of ISM conditions at the time of progenitor star formation.²

Second, and more relevant to our current study, elements such as He, C, N, and s-process elements are found to be enriched in PN, and so measurements of their abundances provide valuable information about the nucleosynthesis that occurs during the lifetime of PN progenitor stars. Figs 1–3 are plots showing He/H, $\log(\text{C}/\text{O})$, and $\log(\text{N}/\text{O})$, respectively, versus $12+\log(\text{O}/\text{H})$, where O/H is taken as the gauge of overall metallicity. Each plot contrasts the values for PN (open symbols) with analogous values of objects such as H II regions and F and G dwarfs, all of which measure the interstellar values of the two ratios involved either currently (H II regions) or at the time of their formation (stars). Original data for the Milky Way Galaxy (MWG) disc PN points in these three figures can be found

¹ The alpha elements O, Ne, S, and Ar are apparently forged in massive stars by similar nuclear processes which transcend position and environment. Therefore, their relative abundances track each other.

² We qualify this seemingly tidy picture by pointing out that oxygen enrichment in PN has been reported by Péquignot et al. (2000) and more recently in C-rich PN by Delgado-Inglada et al. (2015) and García-Hernández et al. (2016).

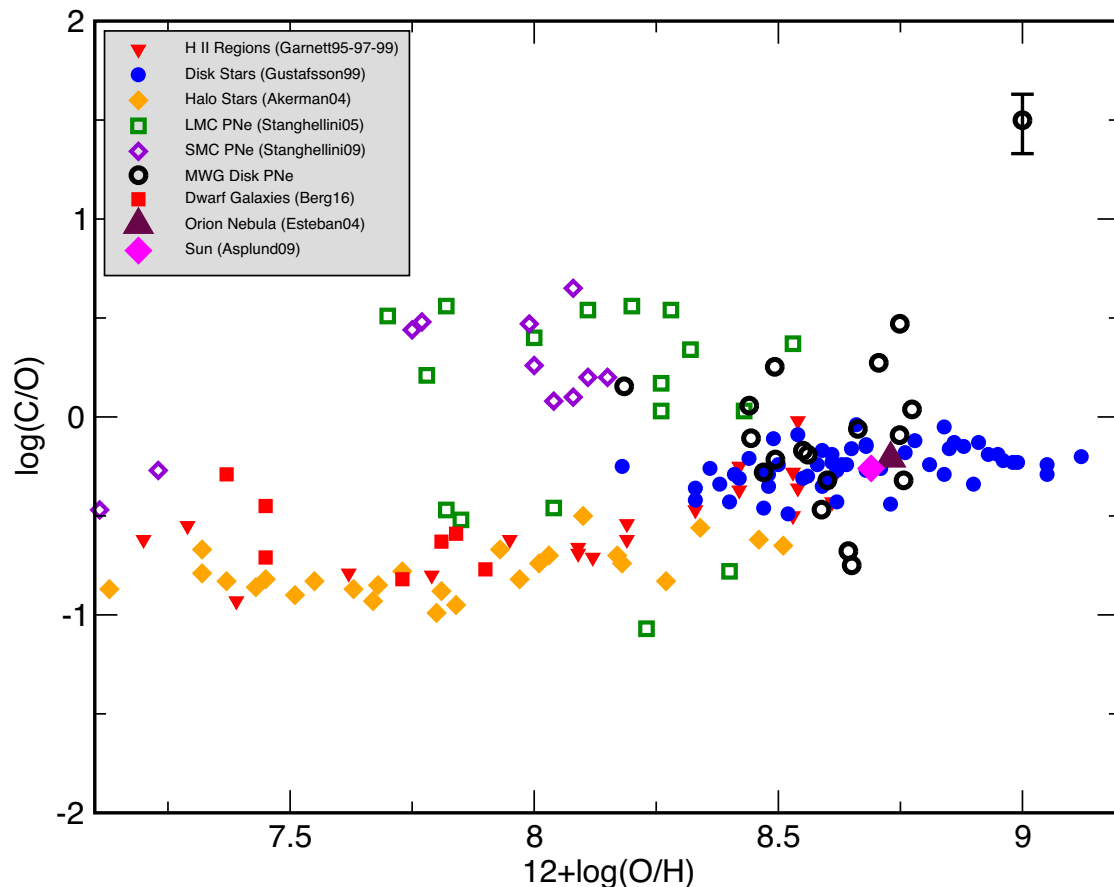


Figure 2. $\log(\text{C}/\text{O})$ versus $12+\log(\text{O}/\text{H})$. Open black circles refer to PN located in the MWG disc and taken from our extended sample, red filled down triangles represent H II regions from Garnett et al. (1995, 1997, 1999), MWG disc stars from Gustafsson et al. (1999) are shown with blue filled circles, MWG metal-poor halo stars from Akerman et al. (2004) are indicated with orange filled diamonds, green open squares and diamonds indicate Large and Small Magellanic Cloud PN by Stanghellini, Shaw & Gilmore (2005) and Stanghellini et al. (2009), respectively, and red filled squares correspond to low-metallicity dwarf galaxies by Berg et al. (2016). The maroon filled up triangle and large magenta filled diamond represent Orion (Esteban et al. 2004) and the Sun (Asplund et al. 2009), respectively.

in Henry et al. (2000), Henry, Kwitter & Balick (2004), Milingo et al. (2010), Kwitter & Henry (2012), and Dufour et al. (2015).

The relatively narrow horizontal band (especially in the cases of C/O and N/O) populated by the H II regions and stars in each graph demonstrates how He/H, C/O, and N/O generally behave as metallicity changes. These patterns of chemical evolution are reflections of the details of stellar evolution and nucleosynthesis, processes which apparently are universal and space invariant. Presumably, when the progenitor stars of the PN in the plots began their lives on the main sequence, they were located along these bands at a position near the PN's current O/H value.

PN values of He/H, C/O, and N/O clearly fall above these bands in nearly every case, strongly suggesting that He, C, and N have been significantly enriched by nucleosynthesis in nearly all progenitor stars over their lifetimes. High PN values for these three abundance ratios have been observed previously. For example, Henry (1990a) compiled the He/H and $\log(\text{N}/\text{O})$ measurements by Aller & Czyzak (1983) and Aller & Keyes (1987) for 84 Galactic PN and found the average values of these two ratios to be 0.11 and -0.38 , respectively. From their large sample of southern PN, Kingsburgh & Barlow (1994) found similar average values for He/H and $\log(\text{N}/\text{O})$ of 0.115 and -0.33 , respectively. In the case of C/O, the log of our average value for objects in the current study (see Table 5) is $\log(\text{C}/\text{O}) = 0.088$ compared with 0.06 from Kingsburgh & Barlow (1994,

see their table 14).³ In addition, simple eyeball comparisons of the ranges of all three ratios shown in Henry (1990a) with Henry (1990b, erratum), the figures in Kingsburgh & Barlow (1994) and our Figs 1–3 in the current paper show good consistency among these studies and reinforce the point that these ratios in PN are generally enhanced relative to levels of found in H II regions of similar metallicity.

Regarding the apparent N enhancement in PN in particular, theory predicts that the hot bottom burning (HBB) process that explains the extent of the enrichment occurs in the AGB stage of stars whose progenitors were at least $3\text{--}4 M_{\odot}$ depending upon the star's metallicity. Yet, based upon the properties of the stellar initial mass function, we also know that in the absence of an unknown selection effect, most of the PN included in these figures must be the products of relatively low-mass progenitors, i.e. $1\text{--}2 M_{\odot}$ and should therefore show very little N enrichment. How can we reconcile this observational result with theory?

The purpose of our investigation here is to confront recently published stellar model predictions of PN abundances with the observed abundances of He, C, N, and O. We consider the models of four

³ Note that we have estimated their averages for N/O and C/O from their separate averages of N, C, and O.

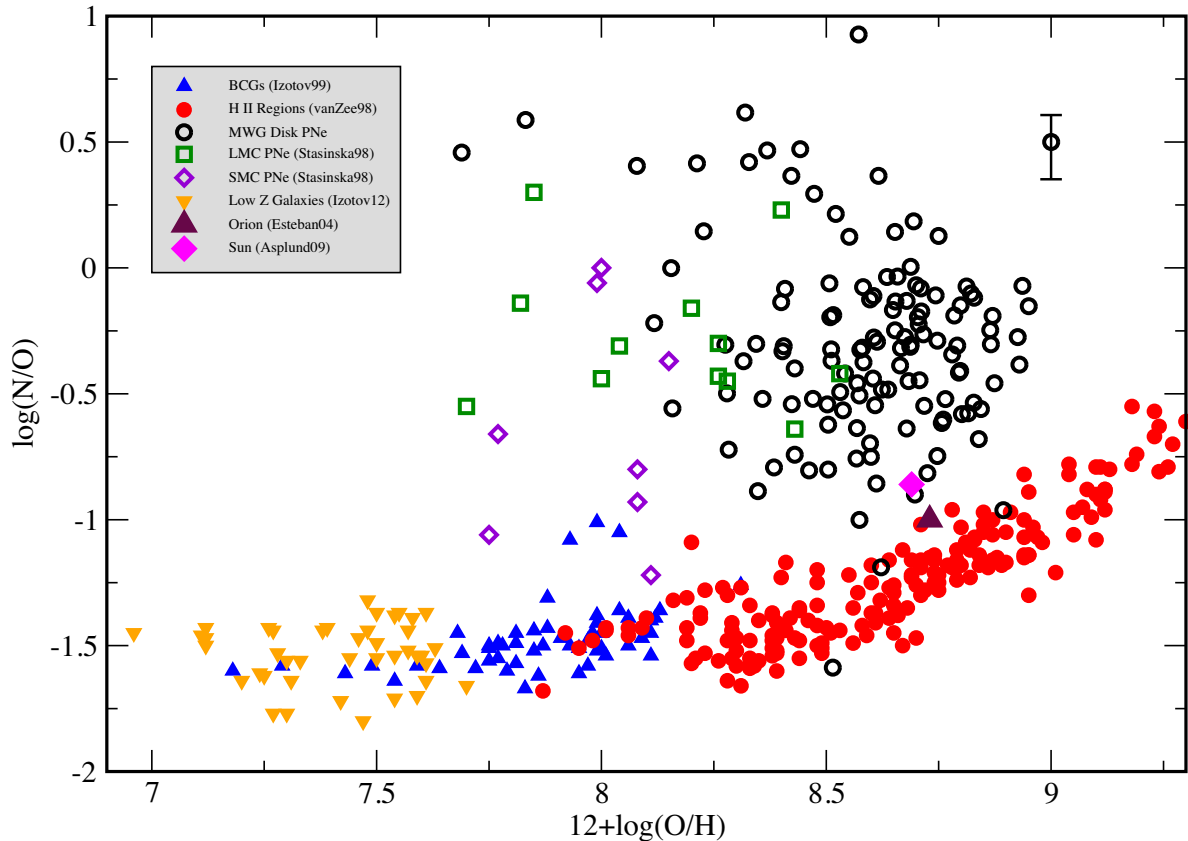


Figure 3. $\log(\text{N}/\text{O})$ versus $12+\log(\text{O}/\text{H})$. Open black circles refer to PN located in the MWG disc and taken from our extended sample, filled blue up triangles represent blue compact galaxies (Izotov & Thuan 1999), filled red circles are H II regions (van Zee et al. 1998), open green squares and open maroon diamonds are PN from the Large and Small Magellanic Cloud, respectively, from Stasińska, Richer & McCall (1998), and filled orange down triangles are low-metallicity galaxies from Izotov, Thuan & Guseva (2012). The maroon large filled up triangle and magenta filled diamond represent Orion (Esteban et al. 2004) and the Sun (Asplund et al. 2009), respectively.

different research groups and evaluate each set of models based upon how well they appear to explain the observed abundances. Since these same models also predict the total stellar yield of each element, only a fraction of which is present in the visible nebula, our results can be used to assess the relevance of the yield predictions for use in chemical evolution models.

Previous studies comparing model predictions and observations have been carried out by Marigo et al. (2003, 2011), Stanghellini et al. (2009), Delgado-Inglada et al. (2015), Ventura et al. (2015), Lugaro et al. (2016), and García-Hernández et al. (2016). The principle method of comparison for these studies features plots of two different element-to-element ratios, e.g. C/O versus N/O, showing both the observed abundances and model tracks computed for a range of stellar masses. Most authors find that abundance trends involving He, C, and N can be explained by various amounts of third dredge up (TDU), which elevates C, and HBB, which does likewise to N. However, explanations of PN abundance patterns based upon progenitor masses is typically not included.

Our study augments earlier analyses by also considering each of the ratios of He/H, C/O, or N/O separately as a function of an object's progenitor mass. The sample of PN abundances which we compare to model predictions consists of 35 objects that have previously been observed and analysed by our group. We have observed all objects in the optical with ground-based telescopes and 13 out of the 35 PN in the UV using either *International Ultraviolet Explorer* (IUE) or *Hubble Space Telescope* (HST).

We describe the PN sample in detail in Section 2. Our methods for determining the necessary abundances and progenitor mass for each object are provided in Section 3. A description of each stellar modelling code used to predict the PN abundances and stellar yields of He, C, and N, along with an analysis of our comparison of theory and observation are presented in Section 4. Our summary and conclusions appear in Section 5.

2 OBJECT SAMPLE

For nearly 25 yr our team has been building a spectroscopic data base comprising 166 PNe located primarily in the disc and halo of the MWG. While a vast majority of the observations have necessarily been restricted to the optical region of the spectrum, i.e. 3700 to 10 000 Å, we have also collected UV data for a smaller sample using both the *IUE* and *HST* facilities. Most of these data, along with derived abundances of He, N, O, Ne, S, Ar, and in several cases C, have been published. Because we are currently interested in comparing our observed CNO abundances in PN with theoretical predictions of the abundances of these same elements as a function of initial stellar mass, it is necessary to identify a subset of our data base for which we can infer progenitor star masses that are based upon carefully and consistently determined central star luminosities and effective temperatures.

Initial stellar masses can be derived by using published values for T_{eff} and $\log(L/L_{\odot})$ of each central star to place the star in

Table 1. Sample objects.

PN	Morphology	Peimbert type	Spectral range ^a	R_G (kpc) ^b	z (pc) ^c
FG1	Elliptical; bipolar jets	II	OP	7.56	251.07
IC2149	Round/complex	II	OP	8.46	276.46
IC2165	Elliptical	II	<i>HST</i> ,OP	9.98	− 536.80
IC3568	Round	II	<i>HST</i> ,OP	9.53	1642.47
IC418	Elliptical	II	<i>IUE</i> ,OP	8.92	− 493.40
IC4593	Elliptical	II	<i>IUE</i> ,OP	6.94	1026.64
N1501	Elliptical	II	OP	8.59	82.12
N2371	Barrel	II	OP	9.31	478.51
N2392	Elliptical	II	<i>IUE</i> ,OP	9.17	382.74
N2438	Round	II	OP	8.95	102.01
N2440	Pinched-waist/multisymmetric	I	<i>HST</i> ,OP	9.23	80.22
N2792	Round	II	OP	8.39	144.41
N3195	Barrel	I	OP	7.35	− 688.73
N3211	Elliptical	II	OP	7.69	− 162.14
N3242	Elliptical/shells/ansae	II	<i>HST</i> ,OP	8.18	530.62
N3918	Barrel	II	OP	7.42	151.08
N5315	Elliptical/multisymmetric	I	<i>HST</i> ,OP	6.93	− 80.02
N5882	Elliptical/shells	II	<i>HST</i> ,OP	6.64	297.52
N6369	Round/shells	II	OP	6.46	157.97
N6445	Irregular/lobe remnants	I	OP	6.63	94.78
N6537	Pinched-waist	I	OP	6.04	25.83
N6563	Elliptical/lobes	II	OP	6.34	− 213.34
N6567	Unresolved	II	OP	6.36	− 19.06
N6572	Elliptical/multisymmetric/lobes	I	OP	6.58	381.92
N6629	Elliptical/halo	II	OP	6.04	− 176.04
N6751	Round/flocculent	I	OP	6.34	− 206.96
N6804	Barrel/shell	II	OP	7.06	− 117.63
N6826	Elliptical/shell/halo/ansae	II	<i>IUE</i> ,OP	7.96	287.77
N6894	Round	I	OP	7.64	− 59.88
N7008	Elliptical	II	OP	8.07	66.97
N7009	Elliptical/shell/halo/ansae	II	<i>IUE</i> ,OP	7.09	− 822.70
N7027	Elliptical/multisymmetric/hourglass-shell/halo	II	OP	7.97	− 51.89
N7293	Round/shells/bowshocks	I	<i>IUE</i> ,OP	7.90	− 184.75
N7354	Barrel/shell/jets	I	OP	8.62	64.76
N7662	Elliptical/shell/halo	II	<i>HST</i> ,OP	8.42	− 380.96

Notes. ^a*HST* = Hubble Space Telescope; *IUE* = International Ultraviolet Explorer; OP = Ground-based optical telescopes. *HST* observations spanned the UV and optical spectral regions, while the *IUE* covered the UV. The ground-based observations normally extended from 3700 Å to 1 μm.

^b $R_G = \{R_\odot^2 - [\cos(b) \times D]^2 - 2 \times R_\odot \times D \times \cos(l) \times \cos(b)\}^{1/2}$, D is the object's heliocentric distance, R_\odot is the Sun's galactocentric distance of 8 kpc, and l and b are heliocentric galactic coordinates. D , l , and b are taken from Frew (2008).

^c $z = D \times \sin(b)$, where D and b are the object's heliocentric distance and galactic longitude, respectively, and are taken from Frew (2008).

a theoretical HR diagram. After plotting post-AGB evolutionary tracks labelled by mass in the same diagram, stellar masses can be inferred by interpolating between tracks.⁴

The extensive compilation of stellar data by Frew (2008, tables 9.5 and 9.6, each comprising 210 objects) was adopted as our source of T_{eff} and $\log(L/L_\odot)$ for reasons of consistency. A total of 32 objects with N and O abundances from our data base were also listed in the Frew paper. We have also measured C abundances using UV emission lines of C III $\lambda\lambda 1907, 1909$ for 10 of the 32 PN. Besides abundances of N and O, we have determined C abundances

for three other objects in our data base which are not part of the Frew list and have included these objects in order to maximize the sample size for objects with measured C abundances. Thus, our final object list contains 35 PN (about 1/5 of the objects in our original data base), all of which have measured N and O abundances and including 13 objects with measured C abundances. We emphasize the fact that the spectroscopic observations of the 35 PN, as well as the data reductions and abundance analyses, were carried out exclusively by members of our team.

Our final sample of 35 objects is listed in Table 1.⁵ For each PN identified in column 1, we provide a morphological description in

⁴ We are very much aware of the pitfalls of using this method to determine central star and progenitor star masses. Problems stem primarily from the small separation between adjacent model evolutionary tracks in the luminosity–temperature plane that are used to infer these masses, given the uncertainties of the observed values of these two parameters. However, we are confident that in using this method we can at least tell if a progenitor star is inside or outside of a mass range for which theory predicts C enrichment through triple alpha burning and dredge up, or N enrichment through HBB.

⁵ Fg1 and NGC 6826 are the only objects in our sample with any evidence of binary central stars. According to Boffin et al. (2012), Fg1 has a period of 1.2 d. NGC 6826 has a fast rotating central star, which is something that can only be achieved in a merger (De Marco et al. 2015). However, neither of these objects exhibits any abundance peculiarities, according to our data. For now, we have assumed that the presence of a secondary star does not affect our results.

Table 2. Journal of observations.

PN	Observation date	Telescope	Instrument ^a	Exp time B	Exp time R	Offset from CS	Ref ^b
Fg1	1997 March–April	CTIO 1.5 m	Cass spec	1500	900	...	1
IC 2149	2007 January	APO 3.5 m	DIS	90	90	...	2
IC 2165	1996 December; HST Cy 19	KPNO 2.1 m	Goldcam	330	90	...	3,4
IC 3568	1996 May; HST Cy 19	KPNO 2.1 m	Goldcam	120	120	4'' N	5,4
IC 418	1996 December	KPNO 2.1 m	Goldcam	30	440	5'' N	6
IC 4593	1996 May	KPNO 2.1 m	Goldcam	180	600	3'' S	5
NGC 1501	2007 January	APO 3.5 m	DIS	240	240	...	2
NGC 2371	1996 December	KPNO 2.1 m	Goldcam	300	300	9.7'' S, 15.7'' W	3
NGC 2392	1996 December	KPNO 2.1 m	Goldcam	450	2520	14'' S	6
NGC 2438	1996 December	KPNO 2.1 m	Goldcam	300	300	16.3'' N	3
NGC 2440	1996 December	KPNO 2.1 m	Goldcam	100	360	4'' S	3,4
NGC 2792	1997 March–April	CTIO 1.5 m	Cass spec	2400	300	...	1
NGC 3195	1997 March–April	CTIO 1.5 m	Cass spec	1200	900	...	1
NGC 3211	1997 March–April	CTIO 1.5 m	Cass spec	480	600	...	1
NGC 3242	1996 December	KPNO 2.1 m	Goldcam	450	480	8'' S	1,4
NGC 3918	1997 March–April	CTIO 1.5 m	Cass spec	100	720	...	3
NGC 5315	2004 August; HST Cy 19	CTIO 1.5 m	Cass spec	961	855	...	7,4
NGC 5882	1997 March–April; HST Cy 19	CTIO 1.5 m	Cass spec	390	480	...	3,4
NGC 6369	2003 June	KPNO 2.1 m	Goldcam	2000	2200	10'' N	7
NGC 6445	2003 June	KPNO 2.1 m	Goldcam	1200	1200	25'' N	7
NGC 6537	2003 June	KPNO 2.1 m	Goldcam	725	300	...	7
NGC 6563	1997 March–April	CTIO 1.5 m	Cass spec	1200	600	...	1
NGC 6567	1997 March–April	CTIO 1.5 m	Cass spec	390	330	...	3
NGC 6572	1999 June	KPNO 2.1 m	Goldcam	72	72	...	8
NGC 6629	1997 March–April	CTIO 1.5 m	Cass spec	420	360	...	1
NGC 6751	2003 June	KPNO 2.1 m	Goldcam	1500	1500	6'' S	7
NGC 6804	2003 June	KPNO 2.1 m	Goldcam	1800	5100	10'' S	7
NGC 6826	1996 May	KPNO 2.1 m	Goldcam	240	720	9'' S	5
NGC 6894	1999 June	KPNO 2.1 m	Goldcam	600	960	...	8
NGC 7008	2004 August	KPNO 2.1 m	Goldcam	1200	1926	29'' N, 11'' E	7
NGC 7009	1996 May	KPNO 2.1 m	Goldcam	90	60	9'' S	5
NGC 7027	1996 May	KPNO 2.1 m	Goldcam	25	110	...	3
NGC 7293	1996 December	KPNO 2.1 m	Goldcam	1800	1800	97'' E, 171'' N	9
NGC 7354	2003 June	KPNO 2.1 m	Goldcam	3503	4500	...	7
NGC 7662	1999 June; HST Cy 19	KPNO 2.1 m	Goldcam	90	100	...	3,4

Notes. ^aSlit dimensions width \times length in arcseconds (length oriented E–W) – Cass Spectrograph: 5×320 ; DIS: 2×360 ; Goldcam: 5×285 ; ^bReferences – 1: Milingo et al. (2002); 2: Henry et al. (2010); 3: Kwitter, Henry & Milingo (2003); 4: Dufour et al. (2015); 5: Kwitter & Henry (1998); 6: Henry et al. (2000); 7: Milingo et al. (2010); 8: Kwitter & Henry (2001); 9: Henry, Kwitter & Dufour (1999).

column 2 and the Peimbert type in column 3. Column 4 indicates the spectral range over which we have observed the object (OP = optical and *IUE/HST* = UV data source). Finally, columns 5 and 6 list the galactocentric distance in kiloparsecs and the vertical height in parsecs above the Galactic plane for each object. Taking the distance of the Sun from the Galactic centre as 8 kpc and the scaleheight of the thin disc as about 350 pc, we see that most of the PN in our sample are located near the solar neighbourhood and within the thin disc. We also note that while the values of the He/H, C/O, and N/O abundance ratios over the MW disc are sensitive to metallicity as measured by O/H, the O/H ratio only decreases by 0.23 dex between 6 and 10 kpc in galactocentric distance, assuming an O/H gradient of -0.058 dex kpc^{-1} (Henry et al. 2010). From Figs 1–3, this corresponds to only minor changes in He/H, C/O, and N/O, and so we can ignore the effects of the disc’s metallicity gradient.

Table 2 provides the details concerning the observations of each of our 35 sample objects. The name of the PN appears in column 1.

Columns 2–7 list the observation date, the telescope(s) and instrument(s) used, the times for the blue and red exposures, and the offset from the central star, respectively. The relevant references for the observations are given in column 8.

Beginning with our first project in 1993, all data have been reduced and measured manually by one of us (KBK) using the same techniques throughout. Uncertainties were explicitly measured and calculated in our early papers; then experience taught us that we could estimate them from the line strengths themselves. ELSA (Emission Line Spectral Analysis, see Section 3.1) calculates statistical uncertainties, but no systematics are included. The former are then propagated through to the final intensities and diagnostics. Systematic errors are minimized by employing the same set of atomic data for abundance determinations throughout and by having a homogeneous data reduction and measuring pipeline, all performed by the same individual. The original line strengths are available in the relevant papers provided in Table 2.

Table 3. Ionic abundance.

PN	He ⁺	σ He ⁺	He ⁺²	σ He ⁺²	C ⁺²	σ C ⁺²	N ⁺	σ N ⁺	O ⁺	σ O ⁺	O ⁺²	σ O ⁺²
FG1	1.16E-01	1.26E-02	1.37E-02	1.88E-03	1.15E-05	1.40E-06	1.90E-05	5.50E-06	2.69E-04	2.45E-05
IC2149	1.05E-01	1.20E-02	8.32E-05	4.03E-05	5.87E-06	8.00E-07	4.14E-05	9.80E-06	1.79E-04	1.72E-05
IC2165	5.70E-02	7.09E-03	4.90E-02	5.15E-03	1.72E-04	1.30E-05	4.61E-06	1.00E-07	1.27E-05	2.00E-06	1.36E-04	5.00E-06
IC3568	1.14E-01	1.26E-02	3.42E-03	1.33E-04	1.55E-04	2.60E-05	3.92E-07	8.10E-08	8.85E-06	5.46E-06	2.82E-04	1.70E-05
IC418	7.00E-02	8.26E-03	3.58E-04	2.03E-04	3.78E-05	7.00E-06	8.38E-05	2.11E-05	6.90E-05	6.00E-06
IC4593	1.02E-01	1.18E-02	5.40E-04	8.30E-05	8.54E-04	1.21E-04	3.45E-06	9.00E-07	4.38E-05	2.50E-05	3.71E-04	3.01E-05
N1501	8.56E-02	9.30E-03	3.86E-02	5.30E-03	1.95E-06	2.00E-07	9.89E-06	1.94E-06	3.20E-04	2.56E-05
N2371	2.62E-02	2.93E-03	8.03E-02	1.13E-02	9.37E-06	2.25E-06	1.66E-05	9.60E-06	1.36E-04	1.66E-05
N2392	5.80E-02	6.50E-03	2.10E-02	2.91E-03	1.26E-04	5.90E-05	1.37E-06	1.32E-06	2.53E-05	7.50E-06	1.14E-04	1.60E-05
N2438	7.53E-02	1.95E-02	2.08E-02	2.82E-03	2.95E-05	5.90E-06	5.04E-05	2.81E-05	2.72E-04	2.69E-05
N2440	5.35E-02	6.89E-03	7.39E-02	6.72E-03	1.42E-04	1.60E-05	7.46E-05	8.00E-06	4.38E-05	1.50E-05	1.25E-04	7.00E-06
N2792	1.92E-02	2.54E-03	9.16E-02	1.33E-02	3.92E-07	2.96E-07	1.64E-06	9.90E-07	1.11E-04	1.61E-05
N3195	1.24E-01	1.35E-02	1.16E-02	1.62E-03	9.59E-05	1.17E-05	1.49E-04	4.50E-05	3.06E-04	2.66E-05
N3211	3.13E-02	3.71E-03	8.39E-02	1.21E-02	1.22E-06	4.60E-07	4.39E-06	4.21E-06	1.85E-04	2.58E-05
N3242	6.88E-02	1.09E-02	4.58E-02	3.77E-03	1.65E-04	8.00E-06	5.72E-07	5.40E-08	5.42E-06	1.46E-06	2.40E-04	5.00E-06
N3918	7.02E-02	8.78E-03	4.43E-02	6.12E-03	1.00E-05	1.70E-06	1.98E-05	6.00E-06	2.62E-04	3.24E-05
N5315	1.32E-01	1.59E-02	2.22E-04	2.70E-05	1.91E-05	1.70E-06	1.21E-05	3.30E-06	3.47E-04	1.70E-05
N5882	1.03E-01	1.33E-02	6.92E-03	4.65E-04	7.83E-05	2.06E-05	1.81E-06	5.00E-08	5.34E-06	8.90E-07	4.11E-04	3.10E-05
N6369	1.30E-01	1.48E-02	1.65E-03	2.24E-04	1.11E-05	1.40E-06	2.22E-05	5.35E-06	4.72E-04	6.78E-05
N6445	9.73E-02	1.05E-02	4.02E-02	5.50E-03	8.72E-05	1.28E-05	1.01E-04	3.40E-05	3.62E-04	3.92E-05
N6537	9.60E-02	1.44E-02	7.43E-02	1.08E-02	2.89E-05	5.90E-06	3.25E-06	1.08E-06	1.10E-04	1.72E-05
N6563	1.11E-01	1.16E-02	1.50E-02	2.04E-03	5.35E-05	7.40E-06	1.22E-04	4.30E-05	2.80E-04	2.81E-05
N6567	1.01E-01	1.44E-02	1.37E-03	1.08E-02	1.50E-06	3.30E-07	4.80E-06	1.67E-06	2.22E-04	2.38E-05
N6572	1.25E-01	1.50E-02	5.64E-04	1.64E-04	6.89E-06	1.19E-06	7.27E-06	1.70E-06	3.72E-04	3.63E-05
N6629	1.09E-01	1.24E-02	1.03E-03	3.15E-04	2.33E-06	5.50E-07	1.54E-05	7.40E-06	3.93E-04	3.30E-05
N6751	1.36E-01	1.51E-02	4.68E-05	6.20E-06	7.93E-05	2.14E-05	3.17E-04	3.00E-05
N6804	2.10E-02	2.67E-03	8.86E-02	1.27E-02	1.38E-07	9.30E-08	1.04E-06	2.70E-07	1.09E-04	1.46E-05
N6826	1.07E-01	1.38E-02	3.93E-04	1.18E-04	2.01E-06	5.50E-06	1.67E-05	9.70E-06	3.59E-04	3.20E-05
N6894	1.14E-01	1.22E-02	1.55E-02	2.12E-03	7.37E-05	9.60E-06	9.36E-05	2.95E-05	2.61E-04	3.91E-05
N7008	7.80E-02	8.39E-03	7.02E-02	9.79E-03	1.22E-06	2.40E-07	2.15E-06	1.09E-06	3.02E-04	3.07E-05
N7009	1.10E-01	1.26E-02	9.43E-03	9.79E-03	6.89E-04	4.31E-04	8.46E-07	1.09E-07	2.05E-06	4.60E-07	4.85E-04	4.50E-05
N7027	6.16E-02	9.36E-03	4.35E-02	6.11E-03	6.79E-06	1.05E-06	6.65E-06	8.10E-07	1.84E-04	2.50E-05
N7293	1.12E-01	1.41E-02	7.99E-02	4.07E-04	1.84E-04	3.35E-04	5.52E-05	7.42E-06	7.50E-05	5.90E-05	3.40E-04	3.60E-05
N7354	9.02E-02	1.02E-02	3.96E-02	5.44E-03	7.82E-06	1.11E-06	6.38E-06	1.84E-06	3.47E-04	3.56E-05
N7662	6.72E-02	6.18E-03	5.47E-02	7.91E-03	1.28E-04	1.40E-05	5.68E-07	3.50E-08	4.64E-06	1.20E-06	1.95E-04	1.00E-05

3 METHODS

3.1 Nebular abundances

We have published abundances of He, N, O, and in some cases C previously in papers indicated in the footnote to column 8 in Table 2. However, we sought to render the abundances more homogeneous by recomputing all of them using the same updated abundance code along with the newly published ionization correction factors (ICFs) by Delgado-Inglada, Morisset & Stasińska (2014) in the cases of total He, C, and O abundances.

Ionic abundances were determined using the code *ELSA*, a program whose core is a five-level atom routine. Emission line strengths and their uncertainties used as input to *ELSA* were taken from the references listed in Table 2. We used an updated version of the program originally introduced by Johnson et al. (2006), where the major change was the addition of a C III] density diagnostic routine based upon the $\lambda 1907/\lambda 1909$ line strength ratio (C III] $\lambda 1909$ was already included in the program). The important emission lines besides H β that were used in the ionic abundance computations for each object were He I $\lambda 5876$, He II $\lambda 4686$, C III] $\lambda \lambda 1907, 1909$, [N II] $\lambda 6584$, [O II] $\lambda 3727$, [O III] $\lambda 5007$, and [O III] $\lambda 4363$.

The resulting ionic abundances and uncertainties with respect to H⁺ produced by *ELSA* are presented in Table 3. The object names are given in column 1 followed by column pairs containing the abundances and uncertainties for each ion labelled in the header.

Uncertainties for the ionic abundances are computed internally by *ELSA* and are the result of contributions from: (1) the uncertainties in the line strength ratios, e.g. $I_\lambda/I_{H\beta}$; and (2) the uncertainties in the reaction rate coefficients (radiative recombination or collisional excitation rate coefficients) that stem from errors in electron temperature.

Ionic abundances in Table 3 were converted to the total elemental abundance ratios of interest here, i.e. He/H, C/O, N/O, and O/H, by multiplying the value of (He⁺² + He⁺)/H⁺, C⁺²/O⁺², N⁺/O⁺, and (O⁺² + O⁺)/H⁺, respectively, by a relevant ICF. Except in the case of N/O, ICFs and their uncertainties were determined using the schemes of Delgado-Inglada et al. (2014). The ICF value for He/H was taken as unity for each object, since negligible amounts of neutral He are expected to be present in PN (see the next paragraph). On the other hand, the values for the C/O and O/H ICFs along with their uncertainties are different for each object and are therefore provided in Table 4. For N/O, we followed Kingsburgh & Barlow (1994) and Kwitter & Henry (2001) and assumed that N/O = (N⁺/O⁺)⁶.

We have assumed throughout that the contribution of neutral He is negligible in all objects. With the possible exception of IC 418, this is justified by the fact that the O⁺²/O⁺ abundance ratio

⁶ Since the radiation- or density-bounded natures of our PN are unknown, Delgado-Inglada (private communication) recommended that we use this ICF instead of the one published in Delgado-Inglada et al. (2014).

Table 4. ICFs for C/O and O/H^a.

PN	ICF(C/O)	σ ICF(C/O)	ICF(O/H)	σ ICF(O/H)
FG1	1.06	0.17
IC2149	1.00	0.15
IC2165	1.09	0.11	1.50	0.24
IC3568	1.17	0.13	1.02	0.17
IC418	0.64	0.04	1.00	0.11
IC4593	1.06	0.45	1.00	0.16
N1501	1.26	0.21
N2371	2.93	0.46
N2392	0.96	0.08	1.21	0.18
N2438	1.15	0.18
N2440	0.87	0.06	1.84	0.27
N2792	3.99	0.66
N3195	1.05	0.14
N3211	2.68	0.44
N3242	1.19	0.13	1.39	0.23
N3918	1.37	0.22
N5315	1.17	0.13	1.00	0.16
N5882	1.21	0.14	1.04	0.17
N6369	1.01	0.16
N6445	1.23	0.18
N6537	1.45	0.24
N6563	1.07	0.15
N6567	1.01	0.17
N6572	1.00	0.16
N6629	1.01	0.16
N6751	1.00	0.15
N6804	3.65	0.60
N6826	1.15	0.12	1.00	0.16
N6894	1.07	0.15
N7008	1.53	0.25
N7009	1.22	0.14	1.05	0.17
N7027	1.41	0.23
N7293	0.96	0.08	1.04	0.16
N7354	1.25	0.21
N7662	1.19	0.13	1.48	0.24

Notes. ^aICFs for C/O and O/H were determined using the formulae in Delgado-Inglada et al. (2014). For He/H and N/O, we assumed that $\text{He}^{++}/\text{H}^{++} + \text{He}^{+}/\text{H}^{+} = \text{He}/\text{H}$ and $\text{N}^{+}/\text{O}^{+} = \text{N}/\text{O}$, respectively.

is greater than unity (see Table 3), since the ionization potential of O^{+} (35.1eV) greatly exceeds that of He^{0} (24.6eV). Concerning IC 418, Dopita et al. (2017) recently published the results of new high-resolution integral field spectroscopy for this PN. Their observations show both moderate [O II] $\lambda 3727$ and [O III] $\lambda 5007$ strengths, weak [O I] $\lambda 6300$ and no He I $\lambda 4686$, qualitatively similar to the findings in Henry et al. (2000) and Sharpee et al. (2003). Dopita et al. (2017) also construct a detailed nebular model that implies an abundance ratio of $\text{He}/\text{H} = 0.11$, significantly higher than our value of 0.07. Therefore, our neglect of neutral He in IC 418 may be unwarranted, in which case our inferred He abundance may in fact be too low. This uncertainty obviously affects the position of IC 418, currently at $\text{He}/\text{H} = 0.07$, in Figs 7, 10, and 11.

Our final elemental abundances and uncertainties appear in Table 5. Object names are provided in column 1, while column 2 contains our estimate of the progenitor star mass for that object. These masses were inferred according to the method described in the next subsection. Beginning with column 3, pairs of columns list the elemental number abundances and uncertainties for He/H, C/O, N/O, and O/H. The uncertainties were rigorously determined by adding in quadrature the partial uncertainty contributions from each ion involved in the total element computation as well as the

ICF uncertainty.⁷ The results provided in Table 5 will be analysed in detail in Section 4 following our detailed discussion of our method for determining progenitor masses.

3.2 Progenitor star masses

Central star and progenitor masses were estimated by plotting the position of each central star in the $\log(L/L_{\odot})$ – $\log T_{\text{eff}}$ plane along with theoretical post-AGB evolutionary tracks and interpolating between tracks for each of our 35 objects. The values of $\log(L/L_{\odot})$ and $\log T_{\text{eff}}$ were taken from Frew (2008) for 32 of our 35 sample objects. For the three sample objects not included in Frew (2008, IC2165, IC3568, and NGC5315), we assumed the L and T values derived from models in Henry et al. (2015).

We decided to base our analysis on the $\log(L/L_{\odot})$ and $\log T_{\text{eff}}$ values for each of our objects found in Frew (2008) because of the thoroughness of the procedures which he used to obtain these values. In his compilation of $\log(L/L_{\odot})$ values, Frew vetted all published V magnitude estimates for quality and then averaged the best values for each central star. Absolute visual magnitudes were then determined via a distance modulus, where distances were inferred from a new relation developed in Frew (2008) between the $\text{H}\alpha$ surface brightness and nebular radius of a PN. Following the application of a bolometric correction, bolometric magnitudes were converted to solar luminosities. The effective temperature of each central star was determined by Frew using the H and He Zanstra temperature methods in most cases. Table 6 contains our adopted values for $\log(L/L_{\odot})$ and $\log T_{\text{eff}}$ in columns 2 and 3, respectively, for each PN listed in column 1.

We experimented with two sets of post-AGB evolutionary tracks: those by Vassiliadis & Wood (1994, $Z = 0.016$, VW) and Miller Bertolami (2016, $Z = 0.010$, MB). Model sets differing in authorship as well as metallicity were chosen deliberately in order to test the effect upon inferred masses. For each set, we plotted tracks in a separate $\log(L/L_{\odot})$ – $\log T_{\text{eff}}$ diagram and then placed our sample objects in the graph using our adopted values of these two stellar properties listed in Table 6.

Figs 4 and 5 show the positions of our sample objects in a $\log(L/L_{\odot})$ – $\log T_{\text{eff}}$ plane along with the model tracks of VW and MB, respectively. The final/initial mass associated with each track is designated by track colour as defined in each figure's legend. Representative error bars for the observed values, shown in the lower right of each figure, are taken directly from fig. 9.8 of Frew (2008), since uncertainties for individual objects were not provided. Because each track is associated with a specific initial and final mass, we carefully measured each object's displacement from adjacent tracks and interpolated to find the mass values. The resulting initial masses determined in Figs 4 and 5 are listed in columns 4 and 5 of Table 6, respectively. The average of these two masses is listed in column 6 of that table as well as in column 2 of Table 5.

Fig. 6 is a plot of masses from column 5 versus those in column 4 of Table 6. The straight line shows the one-to-one relation. For a vast majority of objects, the progenitor masses (M_i) determined using the MB tracks tend to be smaller than those determined from the VW tracks by about $0.3 M_{\odot}$. This systematic difference is a direct consequence of the higher luminosity of the MB models during the constant luminosity stage resulting from the updated treatment of the evolutionary stages that precede the post-AGB stage. However, this offset is less than our estimated uncertainty of $\pm 0.5 M_{\odot}$ and

⁷ The ICF uncertainty was unavailable in the case of N/O.

Table 5. Total elemental abundances.

PN	M_{ave}/M_{\odot}	He/H	$\sigma(\text{He/H})$	C/O	$\sigma(\text{C/O})$	N/O	$\sigma(\text{N/O})$	O/H	$\sigma(\text{O/H})$
FG1	0.6	0.13	0.01	0.61	0.19	3.07E−04	5.60E−05
IC2149	1.2	0.11	0.01	0.14	0.04	2.20E−04	3.89E−05
IC2165	2.3	0.11	0.01	1.37	0.18	0.36	0.06	2.23E−04	3.66E−05
IC3568	2.5	0.12	0.01	0.65	0.14	0.04	0.03	2.96E−04	5.18E−05
IC418	1.4	0.07	0.01	3.34	1.99	0.45	0.14	1.53E−04	2.74E−05
IC4593	0.7	0.10	0.01	2.43	0.45	0.08	0.05	4.16E−04	7.65E−05
N1501	1.7	0.12	0.01	0.20	0.04	4.15E−04	7.52E−05
N2371	0.6	0.11	0.01	0.56	0.35	4.47E−04	9.04E−05
N2392	1.6	0.08	0.01	1.06	0.54	0.05	0.05	1.68E−04	3.35E−05
N2438	1.8	0.10	0.02	0.59	0.35	3.72E−04	7.27E−05
N2440	2.8	0.13	0.01	0.99	0.14	1.71	0.61	3.10E−04	5.44E−05
N2792	1.2	0.11	0.01	0.24	0.23	4.50E−04	9.81E−05
N3195	2.1	0.14	0.01	0.64	0.21	4.78E−04	8.57E−05
N3211	2.5	0.12	0.01	0.28	0.29	5.08E−04	1.09E−04
N3242	1.2	0.11	0.01	0.82	0.10	0.10	0.03	3.40E−04	5.64E−05
N3918	2	0.11	0.01	0.51	0.18	3.85E−04	7.68E−05
N5315	2.4	0.13	0.02	0.75	0.09	1.58	0.45	3.59E−04	6.11E−05
N5882	1.1	0.11	0.01	0.23	0.07	0.34	0.06	4.32E−04	7.81E−05
N6369	3	0.13	0.01	0.50	0.14	4.98E−04	1.06E−04
N6445	2.3	0.14	0.01	0.87	0.32	5.73E−04	1.06E−04
N6537	3.7	0.17	0.02	8.84	3.47	1.65E−04	3.67E−05
N6563	1.7	0.13	0.01	0.44	0.17	4.32E−04	8.17E−05
N6567	0.7	0.10	0.02	0.31	0.13	2.28E−04	4.46E−05
N6572	1.4	0.13	0.01	0.95	0.28	3.80E−04	7.20E−05
N6629	1.6	0.11	0.01	0.15	0.08	4.10E−04	7.54E−05
N6751	2.7	0.14	0.02	0.59	0.18	3.96E−04	7.03E−05
N6804	1.4	0.11	0.01	0.12	0.10	4.01E−04	8.48E−05
N6826	1.6	0.11	0.01	1.26	0.47	0.12	0.34	3.76E−04	6.96E−05
N6894	1	0.13	0.01	0.79	0.27	3.81E−04	7.59E−05
N7008	0.7	0.15	0.01	0.57	0.31	4.66E−04	8.99E−05
N7009	1.4	0.12	0.02	1.74	1.16	0.41	0.11	5.10E−04	9.66E−05
N7027	2.7	0.11	0.01	1.02	0.20	2.69E−04	5.63E−05
N7293	2.1	0.12	0.01	0.52	0.91	0.74	0.59	4.31E−04	9.75E−05
N7354	2.5	0.13	0.01	1.22	0.39	4.42E−04	8.51E−05
N7662	1.2	0.12	0.01	0.78	0.13	0.12	0.03	2.95E−04	5.06E−05

therefore is likely insignificant for our purposes here. Interesting exceptions are the five objects with $M_i \lesssim 1 M_{\odot}$, for which the MB tracks are slightly less luminous than those of VW. This leads to significantly higher extrapolated masses ($M_i \sim 0.8 M_{\odot}$) for three of the objects when using the MB tracks, instead of the unrealistically low $M_i \sim 0.5 M_{\odot}$ obtained with the VW tracks.

4 RESULTS AND DISCUSSION

We now present a comparison of observed abundance ratios for our sample objects to several sets of theoretical model predictions of PN abundances in Figs 7–12. Note that in these figures, model tracks differing in metallicity, but produced by the same code share the same line colour. The metallicity of each model follows the code name in the legend and generally increases in value from solid to dashed to dotted line types. Solar abundance values from Asplund et al. (2009) are shown with black dotted lines.

To understand the differences in the predictions of the different theoretical models, and also to extract some physical insight from their comparison with the observations, it is necessary to keep in mind the different physical assumptions of each grid. The evolution of the surface abundances of AGB stellar models is particularly sensitive to the adopted physics on the AGB. In addition, the properties of the stellar models in advanced evolutionary stages, such as the AGB, are affected by the modelling of previous evolutionary stages.

The latter is particularly true regarding the treatment of mixing processes such as rotationally induced mixing or convective boundary mixing (or overshooting) during H- and He-core burning stages.

4.1 Description of the model codes

We now briefly review the treatment of these key ingredients in the four grids adopted here for the comparison: the MONASH grid (Karakas 2014; Karakas & Lugaro 2016), the LPCODE grid (Miller Bertolami 2016), the ATON grid (Ventura et al. 2015; Di Criscienzo et al. 2016), and the FRUITY data base (Cristallo et al. 2011, 2015). While all the models discussed here include an up-to-date treatment of the microphysics, and all of them neglect the impact of rotation, the theoretical models discussed in this section have some key differences in the modelling of winds and convective boundary mixing processes. These differences will affect the predicted evolution and final abundances during the TP-AGB.

Based on the treatment of winds on the AGB, the models can be roughly divided in two groups. On one hand, we have the MONASH and FRUITY models that adopt a single relation between the pulsational period P and the mass-loss rate \dot{M} for both C-rich and O-rich AGB stars. The mass-loss recipe $\dot{M}(P)$ adopted by the MONASH models is the well-known formula by Vassiliadis & Wood (1993, eqs 1, 2, and 5), while the FRUITY models adopt a similar prescription derived by Straniero, Gallino & Cristallo (2006, see their section 5).

Table 6. Progenitor masses.

PN	$\log(L/L_{\odot})^a$	$\log(T_{\text{eff}})^a$	M/M_{\odot} (VW) ^b	M/M_{\odot} (MB) ^c	M_{ave}/M_{\odot}
FG1	3.23	4.9	0.4	0.8	0.6
IC2149	3.66	4.62	1.3	1.2	1.2
IC2165	3.87	5.06	2.3	2.2	2.3
IC3568	3.98	4.71	2.5	2.4	2.5
IC418	3.72	4.58	1.5	1.3	1.4
IC4593	3.41	4.6	0.5	0.9	0.7
N1501	3.66	5.13	1.8	1.5	1.7
N2371	2.98	5	0.5	0.8	0.6
N2392	3.82	4.67	1.8	1.5	1.6
N2438	2.31	5.09	2.0	1.5	1.8
N2440	3.32	5.32	3.0	2.6	2.8
N2792	3.18	5.1	1.3	1.2	1.2
N3195	2.56	5.15	2.2	1.9	2.1
N3211	2.76	5.21	2.6	2.3	2.5
N3242	3.54	4.95	1.2	1.2	1.2
N3918	3.7	5.18	2.0	2.0	2.0
N5315	3.95	4.78	2.5	2.3	2.4
N5882	3.52	4.83	1.0	1.1	1.1
N6369	4.07	4.82	3.1	2.8	3.0
N6445	2.97	5.23	2.4	2.1	2.3
N6537	3.3	5.4	4.2	3.1	3.7
N6563	2.34	5.09	1.9	1.4	1.7
N6567	3.35	4.78	0.5	0.9	0.7
N6572	3.72	4.84	1.5	1.3	1.4
N6629	3.82	4.67	1.8	1.5	1.6
N6751	3.97	5.02	2.7	2.6	2.7
N6804	3.71	4.93	1.6	1.3	1.4
N6826	3.81	4.7	1.7	1.5	1.6
N6894	2.23	5	0.9	1.0	1.0
N7008	3.12	4.99	0.5	0.8	0.7
N7009	3.67	4.94	1.5	1.2	1.4
N7027	3.87	5.24	2.8	2.6	2.7
N7293	1.95	5.04	2.2	2.0	2.1
N7354	3.95	4.98	2.5	2.5	2.5
N7662	3.42	5.05	1.2	1.2	1.2

Notes. ^aAll values for luminosity and effective temperature were taken directly from Frew (2008) except in the cases of IC2165, IC3568, and NGC5315. For those three objects, observed values listed in tables 5 and 6 in Henry et al. (2015) were assumed.

^bMasses determined using the post-AGB tracks by Vassiliadis & Wood (1994).

^cMasses determined using the post-AGB tracks by Miller Bertolami (2016).

On the other hand, we have the implementations by the ATON and LPCODE grids that incorporate a different treatment for the C-rich and the O-rich AGB winds. The ATON code adopts the empirical law by Bloeker (1995, eqs 1 and 16 with $\eta_R = 0.02$) reduced by a factor 50 for the O-rich phase and the theoretical mass-loss rates by Wachter et al. (2008, eqs 1–3) for C-rich winds. The LPCODE models adopt the empirical law by Groenewegen et al. (1998) for the C-rich phase, while winds for the O-rich phase mostly follow the Schröder & Cuntz (2005) law. These laws appear as eqs (1)–(3), and (5) in Miller Bertolami (2016).

Even more important than the treatment of winds is the treatment of convective boundary mixing (or overshooting) during the TP-AGB phase as well as in previous evolutionary stages. Again the models can be roughly separated into two groups regarding the treatment of overshooting during core-burning stages. As before, on the one hand we have the MONASH and FRUITY models that do not include any kind of convective boundary mixing processes on the upper main sequence where stars have convective cores. However, later during the He-core burning stage, FRUITY models include convective boundary mixing in the form of semiconvection

(Cristallo et al. 2011). And while the MONASH models do not include any explicit prescription for convective boundary mixing, a similar result would be expected from their adopted numerical algorithm to search for a neutrally stable point at the outer boundary of the convective core (Lattanzio 1986). On the other hand, the ATON and LPCODE models include overshooting on top of the H-burning core with its extension calibrated to fit the width of the upper main sequence. Both grids keep the same calibrated overshooting for the convective core during the core He-burning stage. From this difference alone in the treatment of convective boundary mixing before the TP-AGB, one should expect TDU and HBB to develop at lower initial masses (M_i) in the ATON and LPCODE models than in the models of the MONASH and FRUITY grids.

Regarding convective boundary mixing on the TP-AGB, two convective boundaries are key for the strength of TDU events during the TP-AGB (see Herwig 2000). These are the boundary mixing at the bottom of the pulse drive convective zone (PDCZ) that develops in the intershell region during the thermal pulses, and the boundary mixing at the bottom of the convective envelope (CE). The inclusion of overshooting at both convective boundaries increases the

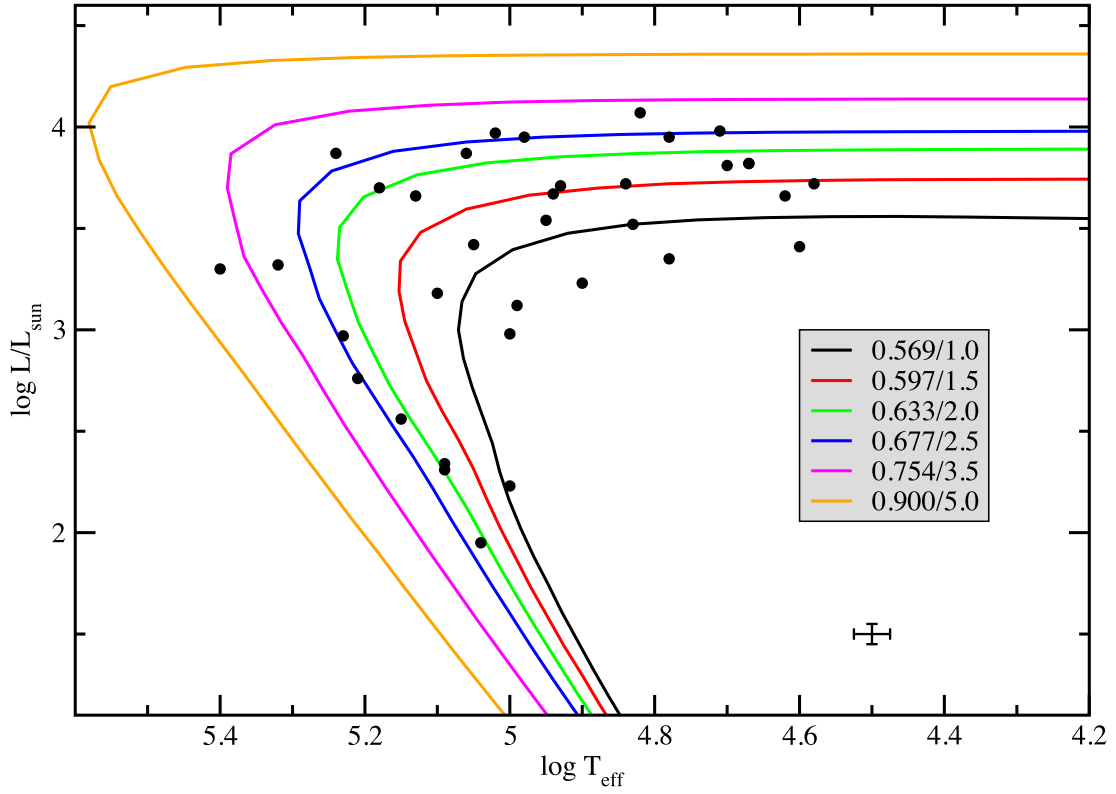


Figure 4. $\log L/L_{\odot}$ versus $\log T_{\text{eff}}$. Solid coloured lines show the post-AGB tracks of Vassiliadis & Wood (1994) for $Z = 0.016$. The legend indicates the correspondence between line colour and remnant/progenitor mass, where stellar mass increases from lower right to upper left. The positions of our 35 objects are shown with filled circles. The representative error bars located in the lower right are taken from fig. 9.8 of Frew (2008).

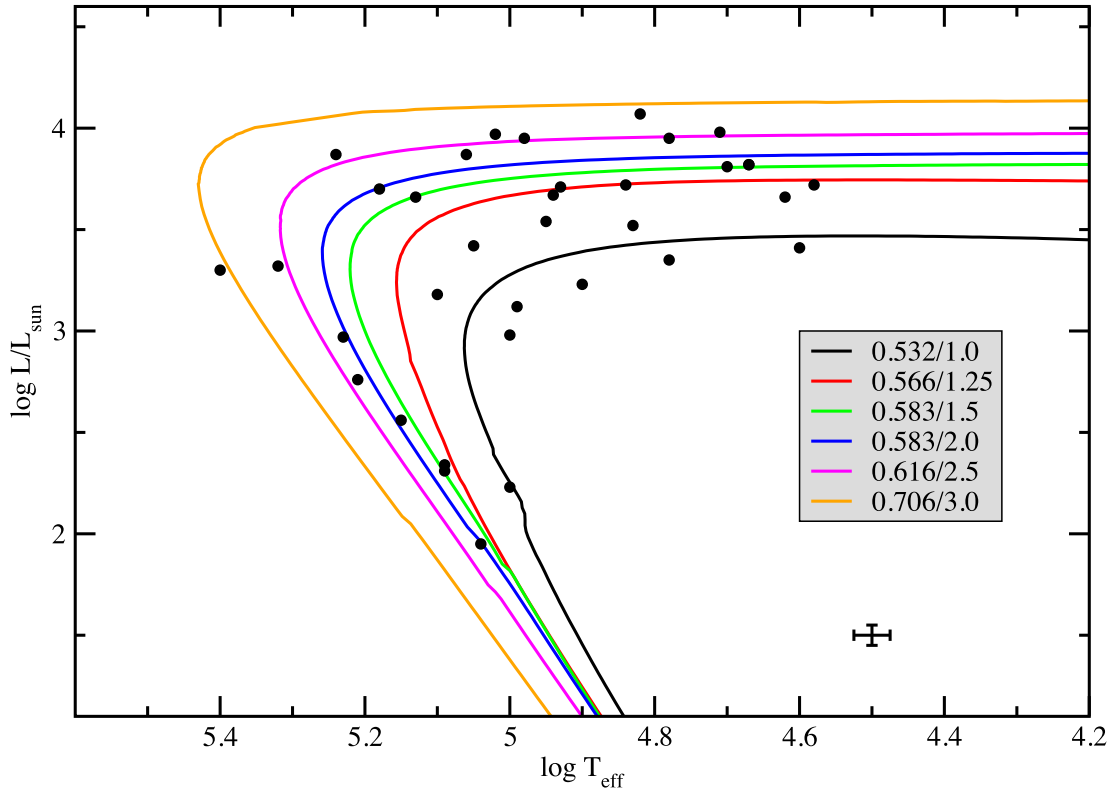


Figure 5. $\log L/L_{\odot}$ versus $\log T_{\text{eff}}$. Solid coloured lines show the post-AGB tracks of Miller Bertolami (2016) for $Z = 0.010$. The legend indicates the correspondence between line colour and remnant/progenitor mass, where stellar mass increases from lower right to upper left. The positions of our 35 objects are shown with filled circles. The representative error bars located in the lower right are taken from fig. 9.8 of Frew (2008).

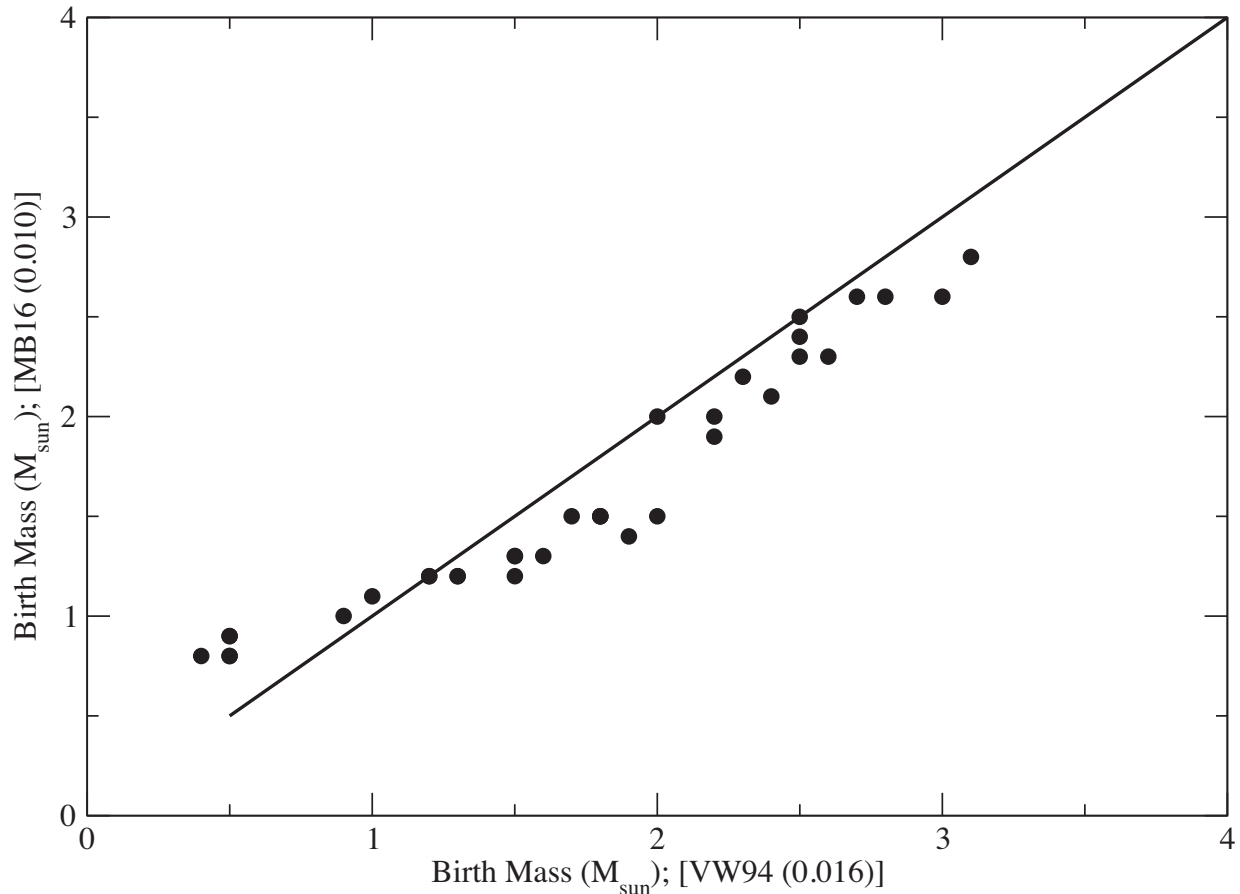


Figure 6. Comparison of progenitor masses of our sample objects derived from the post-AGB tracks of Miller Bertolami (2016) (Fig. 5, vertical axis) and Vassiliadis & Wood (1994) (Fig. 4, horizontal axis). The solid line indicates the one-to-one correspondence.

efficiency of TDU and lowers the threshold in initial stellar mass above which TDU develops. In addition, the inclusion of overshooting at the bottom of the PDCZ leads to the dredging up of O from the CO core, increasing the intershell and surface O abundances.

The treatment of these convective boundaries varies widely in the four grids discussed here. The MONASH models do not include any explicit prescription for convective boundary mixing. However, some overshooting at convective boundaries does occur as a consequence of the adoption of the numerical algorithm for the determination of the convective boundaries (Lattanzio 1986). On the contrary the FRUITY, ATON, and LPCODE models adopt different implementations of an exponentially decaying mixing coefficient (Freitag, Ludwig & Steffen 1996) beyond the formally convective boundaries and with different intensities. While FRUITY models include strong overshooting at the bottom of the CE but no overshooting at the PDCZ, LPCODE models adopt a moderate overshooting at the base of the PDCZ and no overshooting at the bottom of the CE. Finally, the ATON models adopt a very small amount of overshooting both at the bottom of the PDCZ and the CE.

While there are strong arguments in favour of the inclusion of moderate overshooting during the main sequence (Schaller et al. 1992; Pietrinferni et al. 2004; Weiss & Ferguson 2009; Ekström et al. 2012), the situation on the AGB is much less clear. In fact, trying to fit all available observational constraints by means of a simple overshooting prescription might not be even possible (see Weiss & Ferguson 2009; Karakas & Lattanzio 2014; Miller Bertolami 2016).

This fact, together with the lack of compelling theoretical arguments and the lack of a common observational benchmark for AGB theoretical evolution models has led authors to the adoption of very different approaches.

Finally, we note that convection in the ATON code is computed with the full spectrum of turbulence convection, which leads to stronger HBB (Ventura & D’Antona 2005) when compared with models that adopt the standard mixing length theory (Cristallo et al. 2011; Karakas & Lugaro 2016; Miller Bertolami 2016).

In summary, we can roughly divide the four grids into two main groups: (1) the MONASH and FRUITY models that neglect convective boundary mixing during the main sequence, do not include overshooting in the PDCZ and adopt a single wind formula for both the C- and O-rich phases; and (2) the ATON and LPCODE models which calibrate overshooting during core H burning to the width of the main sequence, adopt the same overshooting for the core He-burning phase, include some overshooting at the bottom of the PDCZ, and adopt different wind prescriptions for the C- and O-rich phases. Note, however, that all grids adopt different treatments of convective boundary mixing during the TP-AGB.

In addition to the differences in the adopted physics, there is another difference related to the point at which each sequence is terminated. Due to the several convergence problems experienced by stellar models at the end of the AGB, different authors choose to stop their sequences at some point before the end of the AGB, missing the last thermal pulse(s). Although the efficiency of TDU drops at the end of the AGB, some significant changes in the

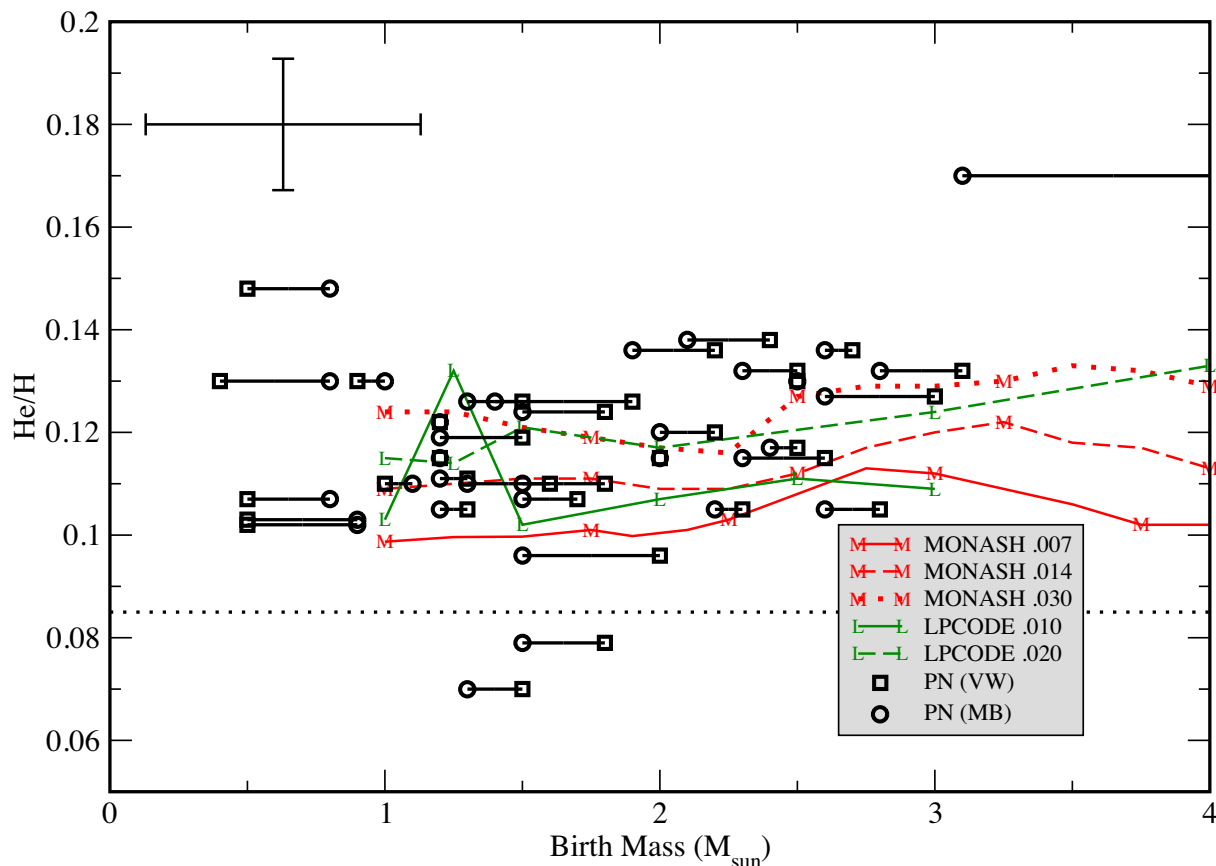


Figure 7. He/H versus central star birth mass in solar units. PNe are shown with connected pairs of open symbols. The squares represent objects whose progenitor masses were determined using the evolutionary tracks of Vassiliadis & Wood (1994, Fig. 4), while the circles similarly refer to the tracks of Miller Bertolami (2016, Fig. 5). Error bars for individual objects have been suppressed for clarity, while a representative set of error bars is provided in the upper left corner of the plot. The horizontal black dotted line indicates the solar He/H value of 0.085 as determined by Asplund et al. (2009). Model predictions by the MONASH (red lines) and LPCODE (green lines) codes are shown for the metallicities given in the legend and designated in the graph by line type.

surface abundances can still happen in the last thermal pulses. This is because when the H-rich envelope mass has already been reduced by more than one order of magnitude, a much smaller amount of processed material needs to be dredged up to the surface to affect the final surface abundances. This is an important difference between the FRUITY, MONASH, and ATON models that do not reach the post-AGB phase and the LPCODE grid models which are computed up until the white dwarf stage. LPCODE models show abundance variations due to the timing of the last AGB thermal pulse.

4.2 Analysis

Our primary results involving the behaviour of He/H, C/O, and N/O versus progenitor mass appear in Figs 7–9. Objects in our sample are shown with connected pairs of open squares and circles. The squares represent objects whose progenitor masses were determined using the evolutionary tracks of Vassiliadis & Wood (1994, our Fig. 4), while the circles similarly refer to the tracks of Miller Bertolami (2016, our Fig. 5). Unpaired green circles represent objects for which the two derived masses were identical. For clarity, only a representative set of error bars is provided in each graph, where the vertical bar indicates the average of the relevant uncertainties given in Table 5. Also included in the plots are model abundance predictions for PN ejecta by the MONASH, LPCODE, ATON, and

FRUITY grids (He/H predictions by the FRUITY and ATON grids were roughly constant at 0.10 and 0.095, respectively, and were not included in Fig. 7). Line colours and types refer to the specific grid and metallicity, respectively, as defined in the figure legend. The horizontal and vertical black dotted lines show the solar values (Asplund et al. 2009).

The behaviour of He/H versus progenitor mass is shown in Fig. 7. Relative to the solar value, all of our sample members except two show He enrichment. Conspicuous outliers include NGC 6537 ($\text{He/H} = 0.17 \pm .02$) in the upper right and IC 418 ($\text{He/H} = 0.07 \pm .01$) and NGC 2392 ($\text{He/H} = 0.08 \pm .01$) both located below the solar line. NGC 6537 is a Peimbert Type I PN, a class which characteristically shows an enhanced He abundance.

Considering the He/H uncertainties, the MONASH and LPCODE model grids span the area occupied by the majority of points. Note, though, that in case of the MONASH models, some of this success is achieved only by including the $Z = 0.030$ model set, i.e. a metallicity roughly twice the solar value. This result is at odds with the metallicities which we measured for our sample of objects, where nearly all have O/H values⁸ in Table 5 at or below

⁸ We note that oxygen may not be a reliable metallicity indicator if significant amounts of O are dredged up to the surface or destroyed by HBB during the TP-AGB as predicted by some models – see section 3.1.1 in Di Criscienzo et al. (2016) and table 3 in Miller Bertolami (2016).

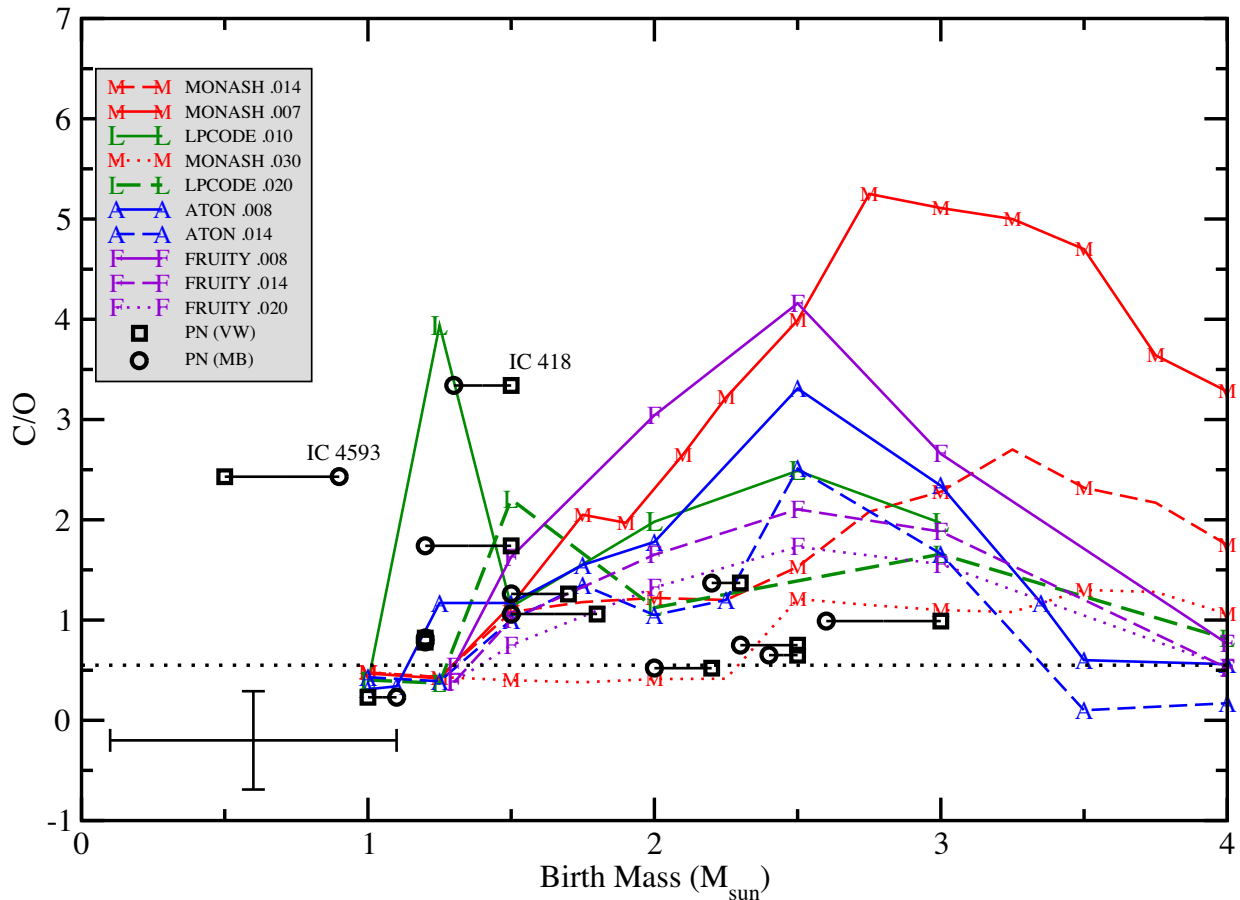


Figure 8. C/O versus central star birth mass in solar units. PNe are shown with connected pairs of open symbols. The squares represent objects whose progenitor masses were determined using the evolutionary tracks of Vassiliadis & Wood (1994, Fig. 4), while the circles similarly refer to the tracks of Miller Bertolami (2016, Fig. 5). Error bars for individual objects have been suppressed for clarity, while a representative set of error bars is provided in the lower left corner of the plot. The horizontal black dotted line indicates the solar C/O value of 0.55 as determined by Asplund et al. (2009). Model predictions by the MONASH (red lines), LPCODE (green lines), ATON (blue lines), and FRUITY (violet lines) codes are shown for the metallicities given in the legend and designated in the graph by line type.

the solar level of 4.90×10^{-4} . In addition both the MONASH and LPCODE models predict a slight rise in He/H with metallicity, but the observational uncertainties of He/H likely obscure this theoretically predicted trend; if it indeed exists, it would be difficult to see it in the data. And while deeper spectra may increase the S/N, accuracy would continue to be compromised due to the errors introduced by flux calibration, dereddening, instrumental effects, and uncertainties associated with atomic constants, including collisional corrections. We feel that uncertainties of no less than ± 0.005 (a vertical error bar of 0.01) could likely be obtained.

In general, the fact that most measured He/H ratios are above the solar value is in line with the expectations from stellar evolution theory, as all dredge-up events during post-main-sequence evolution lead to increases in the He/H ratio. It is well known that extra-mixing processes are needed to explain the abundance patterns in first red giant branch (RGB) stars located above the RGB bump (Charbonnel & Zahn 2007; Charbonnel & Lagarde 2010; Wachlin, Miller Bertolami & Althaus 2011; Lagarde et al. 2012; Maeder et al. 2013). We refer here to mixing processes in addition to overshooting, such

as rotationally induced mixing⁹ or thermohaline mixing.¹⁰ The fact that all grids fail to achieve the maximum observed values of He/H might be related to their neglect of extra-mixing processes on the pre-AGB evolution.

Fig. 8 features the comparison of observations and models pertaining to C/O versus progenitor mass. It is interesting to note that C/O values are centred around 1.23 with a standard deviation of 0.85. Thus, despite the uncertainty in C/O indicated by the

⁹ Rotationally induced mixing includes different types of mixing processes caused by the existence of rotation. These include mixing by meridional circulation and diffusion by shear turbulence in differentially rotating stars (Lagarde et al. 2012; Maeder et al. 2013).

¹⁰ Thermohaline mixing is a double diffusive process that can develop in low-mass stars. This thermohaline instability takes place when the stabilizing agent (heat) diffuses away faster than the destabilizing agent (chemical composition), leading to a slow mixing process. Thermohaline mixing can happen in low-mass stars after the RGB bump, and on the early AGB (Lagarde et al. 2012), where an inversion of molecular weight is created, by the $3\text{He}(3\text{He},2p)4\text{He}$ reaction, on a dynamically stable structure.

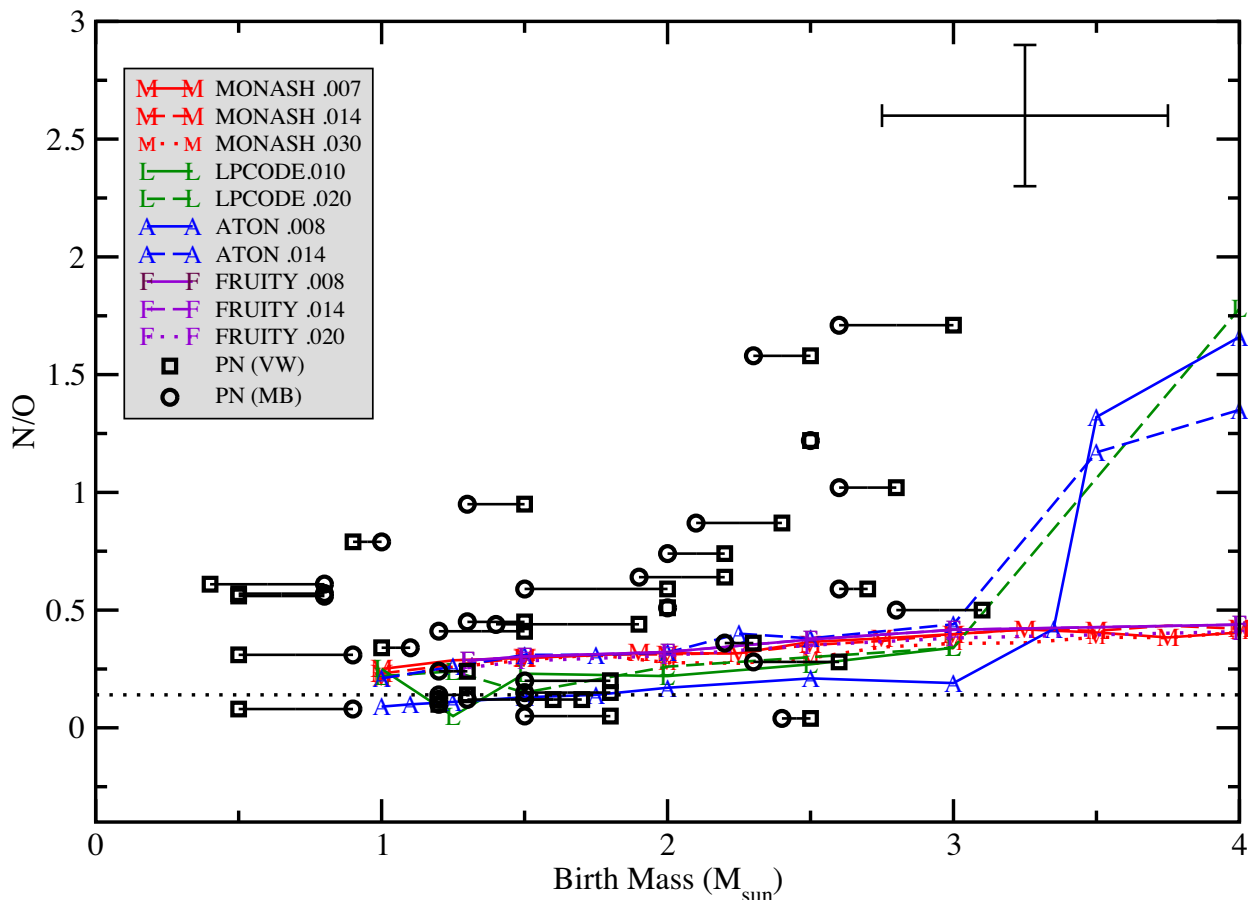


Figure 9. N/O versus central star birth mass in solar units. PNe are shown with connected pairs of open symbols. The squares represent objects whose progenitor masses were determined using the evolutionary tracks of Vassiliadis & Wood (1994, Fig. 4), while the circles similarly refer to the tracks of Miller Bertolami (2016, Fig. 5). Error bars for individual objects have been suppressed for clarity, while a representative set of error bars is provided in the upper right corner of the plot. The horizontal black dotted line indicates the solar N/O value of 0.14 as determined by Asplund et al. (2009). Model predictions by the MONASH (red lines), LPCODE (green lines), ATON (blue lines), and FRUITY (violet lines) codes are shown for the metallicities given in the legend and designated in the graph by line type.

example error bar, the distribution of the 13 objects favours a super-solar value, the result of TDU. Both IC 418 ($C/O = 3.34 \pm 1.99$) and IC 4593 ($C/O = 2.43 \pm .45$) exhibit C/O values which are at least twice the sample average. From our results in Section 3.2 and Table 6, IC 418 had a progenitor mass of roughly $1.4 \pm .5 M_{\odot}$, while IC 4593's mass was originally $0.7 \pm .5 M_{\odot}$. The only model in Fig. 8 which predicts this much excess C within the mass range of the two progenitor stars is the one of $M_i = 1.25 M_{\odot}$ and $Z = 0.010$ in the LPCODE grid. Interestingly, that model attains its high surface carbon abundance due to a final thermal pulse when the mass of the central star is already reduced to $0.593 M_{\odot}$. In this circumstance TDU leads to the mixing of $M_{TDU} \simeq 0.003 M_{\odot}$ from the H-free core into a H-rich envelope of $M_{env}^H \simeq 0.027 M_{\odot}$, significantly increasing the surface carbon abundance of the star. This example shows why it is necessary to keep in mind that final AGB thermal pulses coupled with low envelope masses can significantly change the surface abundances from those predicted by AGB stellar evolution models which are not computed to the very end of the AGB. Yet, it is necessary to emphasize that if the mass ejected after the last thermal pulse is too small, the final abundances of the central stars might be different from those displayed by their surrounding PN. The nebula might not be homogeneous and may be dominated by

the material ejected before the star altered its surface composition in the last thermal pulse.

Each of the four sets of model tracks displayed in Fig. 8 generally predicts two trends regarding C/O in PN: (1) as progenitor mass increases, C/O increases slowly, peaks around $2.5\text{--}3.0 M_{\odot}$ and then decreases; and (2) for constant progenitor mass, C/O increases with decreasing metallicity. Both of these predicted trends are well known and the presumed causes are nicely summarized in Karakas & Lattanzio (2014, section 3.3). In an AGB star, C is produced (and also dredged up from the CO core) within the periodically unstable He shell by the triple-alpha process and is subsequently transported to the H-rich outer envelope during TDU. According to models, the amount of C that is mixed up into the envelope is directly related to the efficiency of the dredge-up process, where the dredge-up efficiency is characterized by the ratio of the mass of material brought to the surface relative to the increase in mass of the C–O core during the process. Models indicate that this efficiency increases independently with increasing progenitor mass and decreasing metallicity. However, this process begins to be damped as the stellar mass approaches $4 M_{\odot}$ in the case of the MONASH grid and $2.5\text{--}3 M_{\odot}$ for the other three grids as C is converted to N via the CN cycle during HBB. The difference between

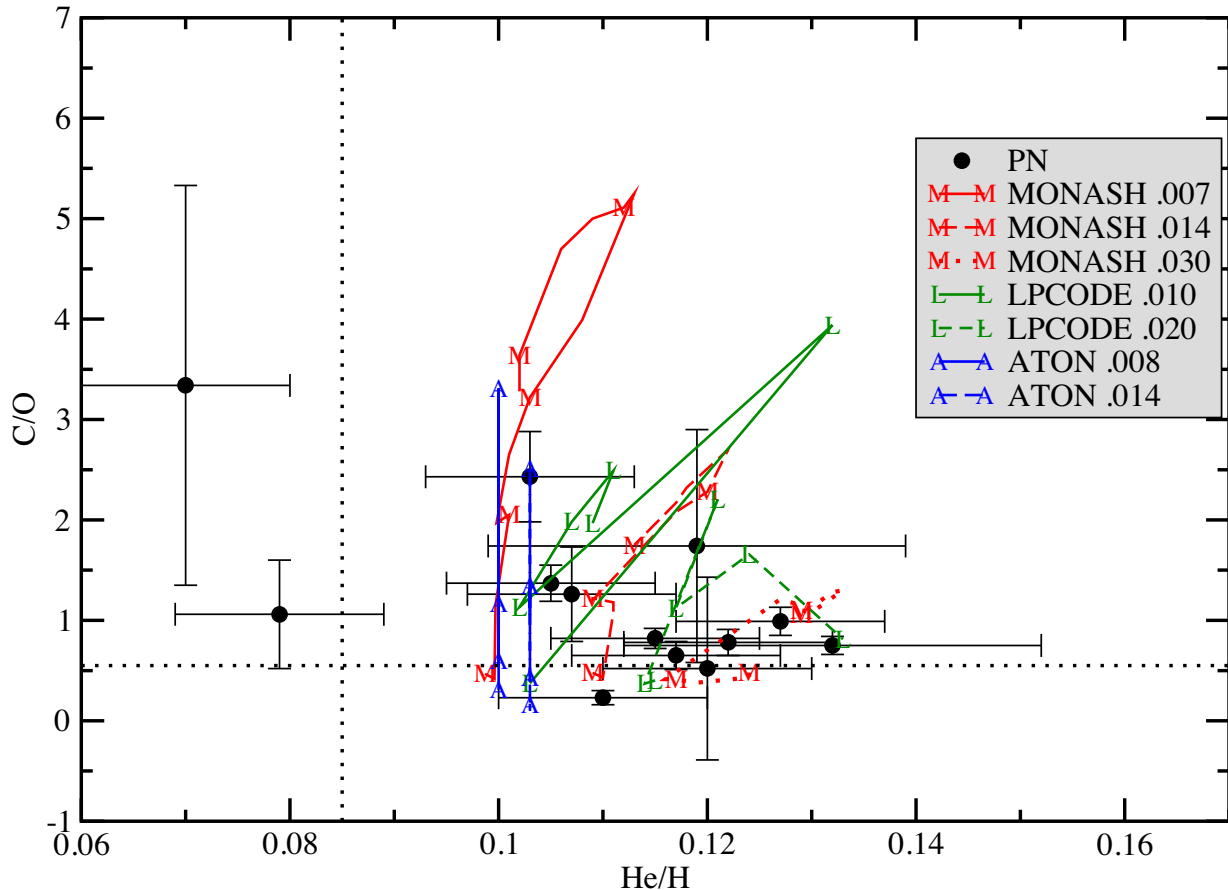


Figure 10. C/O versus He/H. PN are shown with filled black circles. Solar ratios from Asplund et al. (2009) are shown with dotted black lines. Model predictions by the MONASH (red lines), LPCODE (green lines), and ATON (blue lines) codes are shown for the metallicities given in the legend and designated in the graph by line type. Note that the line for the ATON 0.014 model is purposely offset slightly to the right of the ATON 0.008 model to distinguish them, as otherwise they would lie on top of each other.

the MONASH grid and the other three grids could be related to the lack of convective boundary mixing in the high-mass models of the former grid, which leads to a less efficient HBB.

We turn now to the behaviour of N/O versus progenitor mass featured in Fig. 9. Here, we see that roughly 30 per cent of our objects exceed the solar value of 0.14 for N/O by more than their uncertainties. We also observe an upward trend in N/O in the data with increasing birth mass up to about $3 M_{\odot}$.

The apparent nitrogen enrichment below $1.5 M_{\odot}$ is likely the result of dredge-up events before the AGB phase. However, the upward trend beyond this point is rather substantial and likely is the product of HBB. Interestingly, the lowest mass at which HBB is predicted by the ATON and LPCODE models to begin is around $3 M_{\odot}$, while MONASH and FRUITY models predict the onset of HBB at around $5 M_{\odot}$ (outside of the figure range). This difference is mostly due to the implementation of overshooting during the main-sequence evolution in ATON and LPCODE models.

Yet, the upward trend of N/O in our PN sample occurs at an even lower progenitor mass, with high N/O values corresponding to $M_i \gtrsim 2.25 M_{\odot}$. If our stellar mass determinations are reasonably correct, this result confirms the well-established need to include overshooting in the modelling of the upper main sequence, and perhaps the need to include some additional mixing processes like rotation-induced mixing in main-sequence intermediate-mass stars (Ekström et al. 2012, fig. 9).

An additional shortcoming of the models is that none of the sets spans the entire region occupied by our PN. In particular, the observations clearly suggest that stars with progenitor masses below $3 M_{\odot}$ produce higher levels of N than are predicted by any of the models. As mentioned above, the failure of the models to account for the observed abundances of N in low-mass stars might be pointing to the need to include other mixing processes, such as rotation-induced mixing, during previous evolutionary stages (Charbonnel & Lagarde 2010).

Figs 10–12 compare observations and models in terms of one element ratio versus another one. Model tracks apply only to progenitor masses between 1 and 4 solar masses.

Fig. 10 is a plot of C/O versus He/H, where we observe no apparent correlation between the values of these two ratios. As we saw earlier in Fig. 8, the observed He/H ratio for all but IC 418 and NGC 2392 is above the solar value. This strongly suggests that a majority of the objects in our sample experienced significant He enrichment during their evolution. All of the ATON models within the $1\text{--}4 M_{\odot}$ range predict a He/H value of 0.10, hence the straight vertical lines for those models. We have offset their track for the 0.014 metallicity models to the right slightly to help distinguish the two tracks. The model tracks of the MONASH and LPCODE grids are consistent with the observations in the sense that each model set spans the space occupied by the bulk of the sample objects, i.e. those 11 PN which have $\text{He/H} \geq 0.10$. The ATON models appear to

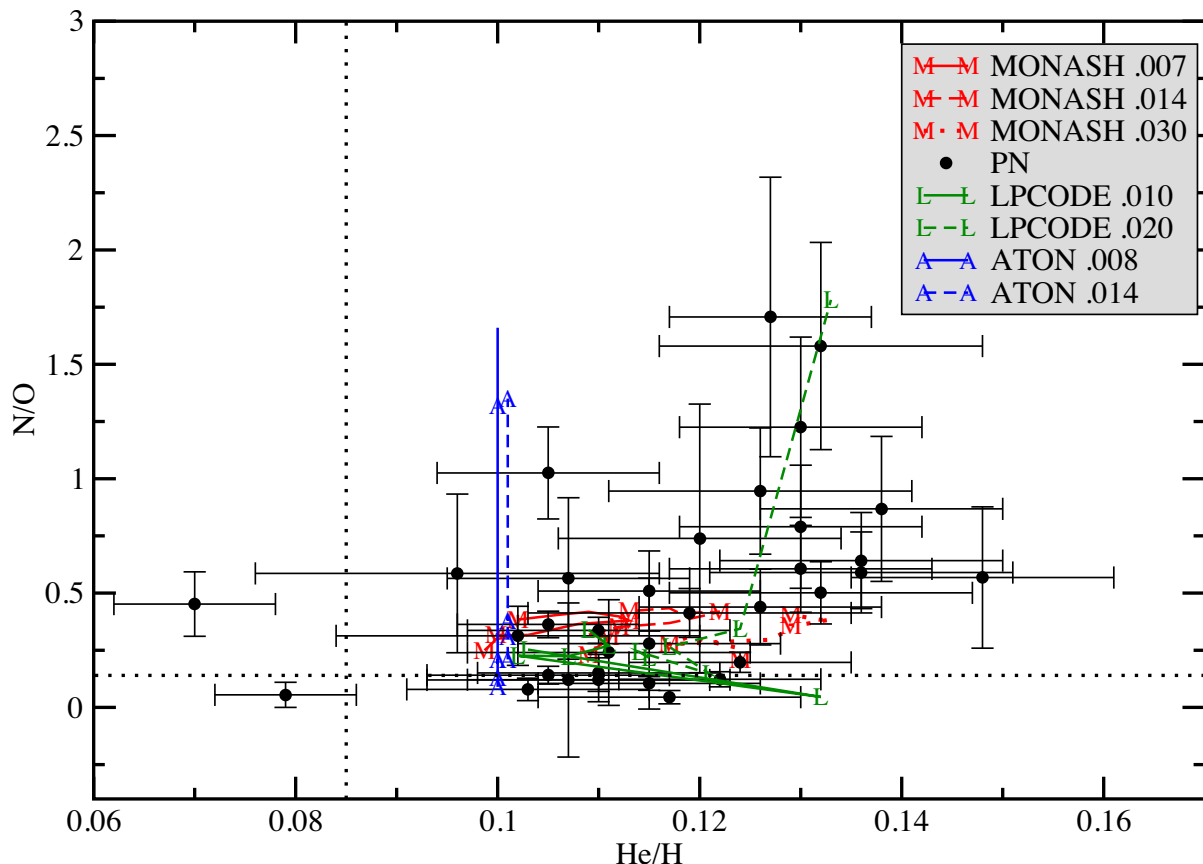


Figure 11. N/O versus He/H. PNe are shown with filled circles. Solar ratios from Asplund et al. (2009) are shown with dotted black lines. Model predictions by the MONASH (red lines), LPCODE (green lines), and ATON (blue lines) codes are shown for the metallicities given in the legend and designated in the graph by line type. Note that the line for the ATON 0.014 model is purposely offset slightly to the right of the ATON 0.008 model to distinguish them, as otherwise they would lie on top of each other.

span the observed C/O values, but lack the range in He/H exhibited by the data.

The observational data in Fig. 11 suggest that the N enrichment seen earlier in Fig. 9 may be coupled with He enrichment in the sense that large N/O values occur at high levels of He/H, although the large uncertainties in both N/O and He/H cloud the issue. Interestingly, a clear positive trend in N/O versus O/H was reported by Kaler (1979) for Galactic disc PN, while Kingsburgh & Barlow (1994) observed similar behaviour in Type I PN only. The MONASH models fail to predict such behaviour, as does the $Z = 0.01$ LPCODE model track. This is due to the lack of efficient HBB in these models, as the MONASH models do not show HBB for $M_i < 4 M_\odot$ and the LPCODE grid only reaches $M_i = 3 M_\odot$ for this grid. On the contrary, LPCODE models with $Z = 0.02$ do show an upward trend in N/O as He/H increases due to the action of TDU and HBB during a large number of thermal pulses in the $M_i = 4 M_\odot$ model. The ATON models seem to span the observed N/O values, although again there is no reported range in their He/H values. Overall, there is little theoretical evidence that any of the model grids completely spans the point positions of the observational data, the result we also see in Fig. 9. We conclude that the possible observational trend in Fig. 11 previously seen in Fig. 9 is likely reflecting the action of TDU and HBB.

Finally, Fig. 12 shows the relation of C/O versus N/O for the 13 objects for which we have C measurements. As we saw in Fig. 8, these data exhibit a wide variation in the C/O ratio, with several ob-

jects having values significantly larger than the solar value. These same objects also have relatively low values of N/O, where ratios range from near solar to slightly above it. Then, there are the three PN with solar C/O values that appear to be decidedly enriched with N. All model sets predict a significant variation in enhanced C/O at relatively low N/O, while at higher N/O levels the C/O values approach the solar value of 0.55. The data appear to be consistent with the models, and generally speaking, all model sets appear to span the empirical data sufficiently, although the high N/O region contains only three PN. The data in this figure are consistent with the theoretical expectation that C and N are anticorrelated, as C from TDU is subsequently destroyed during HBB to produce N.

Summarizing our detailed comparison of models and observations, the empirical trends seen in Figs 9 and 12, and perhaps Fig. 11, suggest the existence of HBB in stars with birth masses less than $4 M_\odot$, something that is only attained by models that include overshooting on the main sequence (ATON and LPCODE).

In more general terms, however, observations, when combined with model predictions of four independent model grids, currently demonstrate that all four grids are compatible with the data except in the case of N/O. That is, all grids seem capable of spanning the distribution of points in the cases of C/O and He/H. We suggest that future computational efforts consider the implication that the onset of HBB occurs at a lower initial mass than previously believed. This is the most important result of our study.

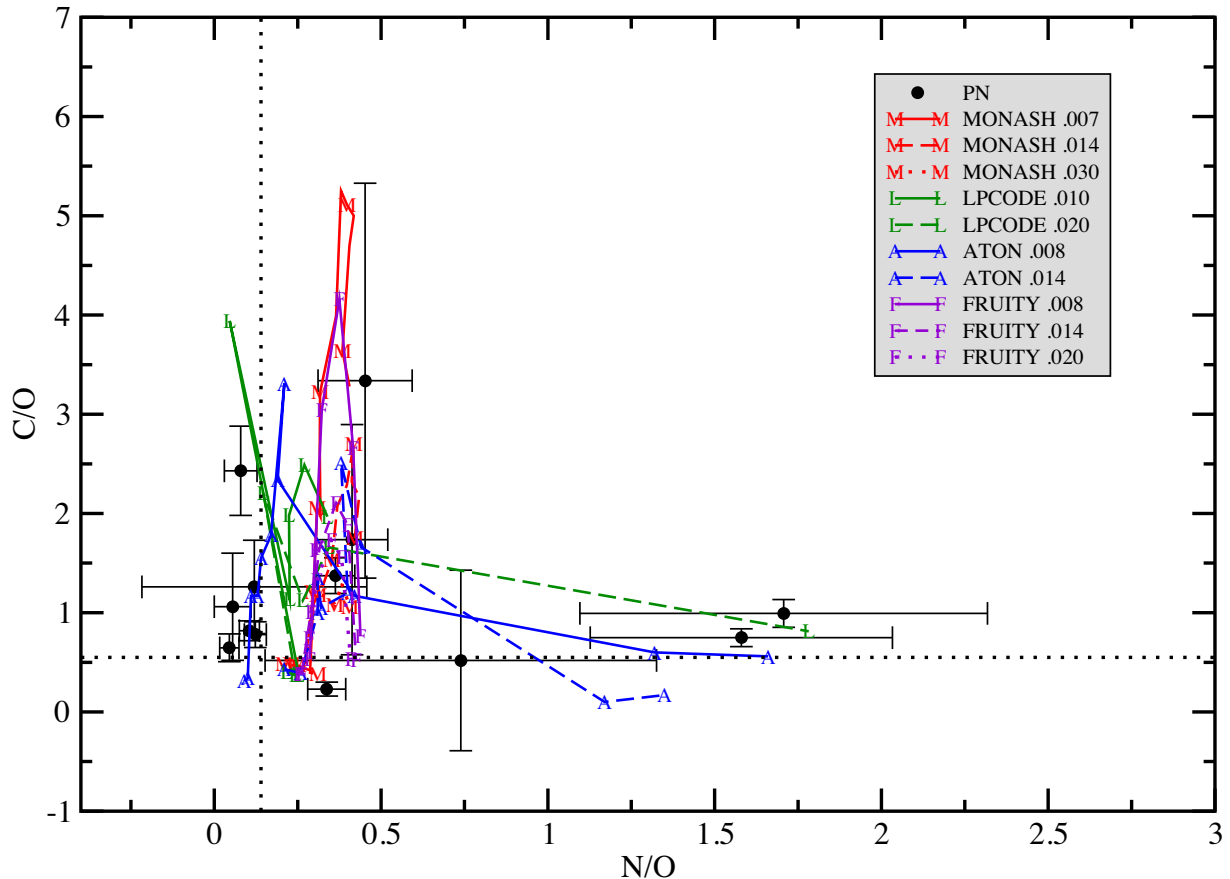


Figure 12. C/O versus N/O. PNe are shown with filled black circles. Solar ratios from Asplund et al. (2009) are shown with dotted black lines. Model predictions by the MONASH (red lines), LPCODE (green lines), ATON (blue lines), and FRUITY (violet lines) codes are shown for the metallicities given in the legend and designated in the graph by line type.

5 SUMMARY AND CONCLUSIONS

Helium, carbon, and nitrogen are known through observations to be synthesized by stars within the mass range of $1\text{--}8\,M_{\odot}$ (LIMS). We demonstrated this plainly in Figs 1–3, where we saw that the He/H, C/O, and N/O abundance ratios as a function of metallicity in a large sample of PN systematically fall above ISM values for the same ratios measured by stars and H II systems.

To evaluate the significance of the relative contribution that LIMS make to the galactic chemical evolution of these three elements, we need to determine the amount of He, C, and N that a star produces and releases into the ISM, i.e. the stellar yield. Fortunately, a portion of this ejected matter forms a PN, and from the emission spectra produced by these objects, we are able to measure the abundances of He, C, and N among other elements. Since theoretical models of LIMS predict both the total yield and the PN abundance, by comparing the observed abundances to theoretical predictions of the same we can simultaneously infer the yield.

The goal of this project has been to make a detailed comparison between observationally determined abundances of the elements He, C, and N in PNe with theoretical predictions of the same by four different grids of stellar evolution models. We have carefully selected PN for which high-quality spectra and good determinations of the luminosity and effective temperature of each associated central star are available. The optical and UV spectra consist exclusively of our own observations made with ground-based telescopes as well as *HST*/ Space Telescope Imaging Spectrograph (STIS) and *IUE*.

To ensure homogeneity, all spectral data were reduced and measured in a consistent manner, and abundances were all determined using the same algorithms. Central star luminosities and effective temperatures in all, but three cases were taken from Frew (2008), and central and progenitor star masses were inferred by plotting these values in $L\text{--}T$ diagrams containing evolutionary tracks from Vassiliadis & Wood (1994) and Miller Bertolami (2016).

Our final sample contained 35 Galactic PN, 13 of which have C abundances measured from UV lines available. These 35 objects vary widely in morphology. All are either categorized as Peimbert type I or II. And most are located in the Galactic thin disc within 2 kpc of the Sun.

Combining the inferred abundances and stellar masses, we conclude the following:

(i) The mean values of N/O across the observed progenitor mass range of $1\text{--}3\,M_{\odot}$ are well above the solar value. With respect to current theory, this is an unexpected result and suggests that extra mixing is required in this stellar group to explain the N enrichment. Our results also suggest an increase in N/O with progenitor mass for $M > 2\,M_{\odot}$, implying that the onset of HBB occurs at lower masses than previously thought.

(ii) All but two of our sample PN clearly show evidence of He enrichment relative to the solar value. This is expected, since both first and TDU mix He-rich material into the stellar atmosphere prior to PN formation from expelled atmospheric matter.

(iii) The average value of measured C/O within our sample is 1.23, well above the solar value of 0.55 (Asplund et al. 2009). The standard deviation for the sample is 0.85. Evidence of C enrichment is present in roughly half of the sample of 13 objects for which we measured the C abundance. Interestingly, the PN with the higher C/O values seem to come from low-mass progenitors with $M \approx 1M_{\odot}$.

(iv) The model grids to which we compared the observations successfully span the data points in the case of C/O. The models are also consistent with some, but not all, of the objects in terms of He/H. However, all of the models seem to fail in the case of N/O.

Our finding of elevated N/O in low-mass stars, possibly due to an earlier-than-expected onset of HBB and/or the presence of extra mixing, is the most significant result of our study. Further confirmation of this result will help markedly in the ongoing efforts to determine the provenance of N in the context of galactic chemical evolution. Because stars of masses between 1 and $3M_{\odot}$ are roughly five times more numerous than stars between 3 and $8M_{\odot}$ (assuming a simple Salpeter initial mass function), the potential impact of these low-mass stars on the question of the chemical evolution of nitrogen is obviously significant.

ACKNOWLEDGEMENTS

The anonymous referee of our paper offered many helpful suggestions for improvement, and we thank him/her for performing such a careful review. We also thank Paolo Ventura and Sergio Cristallo for providing answers to our enquiries regarding the details of the ATON (Ventura) and FRUITY (Cristallo) model predictions and in some cases sending us additional output. We also appreciate the help provided by Gloria Delgado-Inglada concerning her group's recently updated ICFs. Portions of the UV data employed in our project came from *HST* programme number GO12600. BGS is grateful for summer support by the US National Science Foundation (NSF) through the Research Experience for Undergraduates programme. MMBB was supported by ANPCyT through grant PICT-2014-2708 and by a Return Fellowship from the Alexander von Humboldt Foundation. Finally, RBCH, BGS, KBK, and BB are grateful to their home institutions for travel support.

REFERENCES

Akerman C. J., Carigi L., Nissen P. E., Pettini M., Asplund M., 2004, *A&A*, 414, 931
 Aller L. H., Czyzak S. J., 1983, *ApJS*, 51, 211
 Aller L. H., Keyes C. D., 1987, *ApJS*, 65, 405
 Asplund M., Grevesse N., Sauval A. J., Scott P., 2009, *ARA&A*, 47, 481
 Berg D. A., Skillman E. D., Henry R. B. C., Erb, D. K., Carigi L., 2016, *ApJ*, 827, 126
 Bloeker T., 1995, *A&A*, 297, 727
 Boffin H. M. J., Miszalski B., Rauch T., Jones D., Corradi R. L. M., Napiwotzki R., Day-Jones A. C., Köppen J., 2012, *Science*, 338, 773
 Charbonnel C., Lagarde N., 2010, *A&A*, 522, A10
 Charbonnel C., Zahn J.-P., 2007, *A&A*, 467, L15
 Cristallo S. et al., 2011, *ApJS*, 197, 17
 Cristallo S., Straniero O., Piersanti L., Gobrecht D., 2015, *ApJS*, 219, 40
 De Marco O., Long J., Jacoby G. H., Hillwig T., Kronberger M., Howell S. B., Reindl N., Margheim S., 2015, *MNRAS*, 448, 3587
 Deharveng L., Peña M., Caplan J., Costero R., 2000, *MNRAS*, 311, 329
 Delgado-Inglada G., 2016, in Liu X., Stanghellini L., Karakas A., eds, *Proc. IAU Symp. 323, Planetary Nebulae: Multi-wavelength Probes of Stellar and Galactic Evolution*. Kluwer, Dordrecht (arXiv:1611.10246)
 Delgado-Inglada G., Morisset C., Stasińska G., 2014, *MNRAS*, 440, 536

Delgado-Inglada G., Rodríguez M., Peimbert M., Stasińska G., Morisset C., 2015, *MNRAS*, 449, 1797
 Di Criscienzo M. et al., 2016, *MNRAS*, 462, 395
 Dopita M. A., Ali A., Sutherland R. S., Ali A., Sutherland R. S., Nicholls D. C., Amer M. A., 2017, *MNRAS*, 470, 839
 Dufour R. J., Kwitter K. B., Shaw R. A., Henry R. B. C., Balick B., Corradi R. L. M., 2015, *ApJ*, 803, 23
 Ekström S. et al., 2012, *A&A*, 537, A146
 Esteban C., Peimbert M., García-Rojas J., Ruiz M. T., Peimbert A., Rodríguez M., 2004, *MNRAS*, 355, 229
 Frew D., 2008, PhD thesis, Macquarie Univ.
 Freytag B., Ludwig H.-G., Steffen M., 1996, *A&A*, 313, 497
 García-Hernández D. A., Ventura P., Delgado-Inglada G., Dell'Agli F., Di Criscienzo M., Yagüe A., 2016, *MNRAS*, 458, L118
 Garnett D. R., Skillman E. D., Dufour R. J., Peimbert M., Torres-Peimbert S., Terlevich R., Terlevich E., Shields G. A., 1995, *ApJ*, 443, 64
 Garnett D. R., Skillman E. D., Dufour R. J., Shields G. A., 1997, *ApJ*, 481, 174
 Garnett D. R., Shields G. A., Peimbert M., Torres-Peimbert S., Skillman E. D., Dufour R. J., Terlevich E., Terlevich R. J., 1999, *ApJ*, 513, 168
 Groenewegen M. A. T., Whitelock P. A., Smith C. H., Kerschbaum F., 1998, *MNRAS*, 293, 18
 Gustafsson B., Karlsson T., Olsson E., Edvardsson B., Ryde N., 1999, *A&A*, 342, 426
 Henry R. B. C., 1990, *ApJ*, 356, 229
 Henry R. B. C., 1990, *ApJ*, 363, 728
 Henry R. B. C., Kwitter K. B., Dufour R. J., 1999, *ApJ*, 517, 782
 Henry R. B. C., Kwitter K. B., Bates J. A., 2000, *ApJ*, 531, 928
 Henry R. B. C., Kwitter K. B., Balick B., 2004, *AJ*, 127, 2284
 Henry R. B. C., Kwitter K. B., Jaskot A. E., Balick B., Morrison M., Milingo J. B., 2010, *ApJ*, 724, 748
 Henry R. B. C., Balick B., Dufour R. J., Kwitter K. B., Shaw R. A., Miller T. R., Buell J. F., Corradi R. L. M., 2015, *ApJ*, 813, 121
 Herwig F., 2000, *A&A*, 360, 952
 Herwig F., 2005, *ARA&A*, 43, 435
 Izotov Y. I., Thuan T. X., 1999, *ApJ*, 511, 639
 Izotov Y. I., Thuan T. X., Guseva N. G., 2012, *A&A*, 546, A122
 Johnson M. D., Levitt J. S., Henry R. B. C., Kwitter K. B., 2006, in Barlow M. J., Méndez R., eds, *IAU Symp. 234, Planetary Nebulae in our Galaxy and Beyond*. Cambridge Univ. Press, Cambridge, p. 439
 Kaler J. B., 1979, *ApJ*, 228, 163
 Karakas A. I., 2014, *MNRAS*, 445, 347
 Karakas A. I., Lattanzio J. C., 2014, *Publ. Astron. Soc. Aust.*, 31, 30
 Karakas A. I., Lugaro M., 2016, *ApJ*, 825, 26
 Kingsburgh R. L., Barlow M. J., 1994, *MNRAS*, 271, 257
 Kwitter K. B., Henry R. B. C., 1998, *ApJ*, 493, 247
 Kwitter K. B., Henry R. B. C., 2001, *ApJ*, 562, 804
 Kwitter K. B., Henry R. B. C., 2012, in Manchado A., Stanghellini L., Schönberner D., eds, *Proc. IAU Symp. 283, Planetary Nebulae: An Eye to the Future*. Kluwer, Dordrecht, p. 119
 Kwitter K. B., Henry R. B. C., Milingo J. B., 2003, *PASP*, 115, 80
 Lagarde N., Decressin T., Charbonnel C., Eggenberger P., Ekström S., Palacios A., 2012, *A&A*, 543, A108
 Lattanzio J. C., 1986, *ApJ*, 311, 708
 Lugaro M., Karakas A. I., Pignatari M., Doherty C. L., 2016, in Liu X., Stanghellini L., Karakas A. I., eds, *Proc. IAU Symp. 323, Planetary Nebulae: Multi-wavelength Probes of Stellar and Galactic Evolution*. Kluwer, Dordrecht
 Maciel W. J., Costa R. D. D., Cavichia O., 2017, *Rev. Mex. Astron. Astrofis.*, 53, 151
 Maeder A., Meynet G., Lagarde N., Charbonnel C., 2013, *A&A*, 553, A1
 Marigo P., Bernard-Salas J., Pottasch S. R., Tielens A. G. G. M., Wessellius P. R., 2003, *A&A*, 409, 619
 Marigo P., Bressan A., Girardi L., Aringer B., Gullieuszik M., Groenewegen M. A. T., 2011, in Kerschbaum F., Lebzelter T., Whig R. F., eds, *ASP Conf. Ser. 445, Why Galaxies Care About AGB Stars II: Shining*

- Examples and Common Inhabitants. Astron. Soc. Pac., San Francisco, p. 431
- Milingo J. B., Kwitter K. B., Henry R. B. C., Cohen R. E., 2002, *ApJS*, 138, 279
- Milingo J. B., Kwitter K. B., Henry R. B. C., Souza S. P., 2010, *ApJ*, 711, 619
- Milingo J. B., Kwitter K. B., Henry R. B. C., Souza S. P., 2010, *ApJ*, 711, 619
- Miller Bertolami M. M., 2016, *A&A*, 588, A25
- Péquignot D., Walsh J. R., Zijlstra A. A., Dudziak G., 2000, *A&A*, 361, L1
- Pietrinferni A., Cassisi S., Salaris M., Castelli F., 2004, *ApJ*, 612, 168
- Schaller G., Schaerer D., Meynet G., Maeder A., 1992, *A&AS*, 96, 269
- Schröder K.-P., Cuntz M., 2005, *ApJ*, 630, L73
- Sharpee B., Williams R., Baldwin J. A., van Hoof P. A. M., 2003, *ApJS*, 149, 157
- Stanghellini L., Shaw R. A., Gilmore D., 2005, *ApJ*, 622, 294
- Stanghellini L., Lee T.-H., Shaw R. A., Balick B., Villaver E., 2009, *ApJ*, 702, 733
- Stasińska G., Richer M. G., McCall M. L., 1998, *A&A*, 336, 667
- Sterling N. C., 2017, in Liu X., Stanghellini L., Karakas A., eds, *Proc. IAU Symp. 323, Planetary Nebulae: Multi-wavelength Probes of Stellar and Galactic Evolution*. Kluwer, Dordrecht
- Straniero O., Gallino R., Cristallo S., 2006, *Nucl. Phys. A*, 777, 311
- van Zee L., Salzer J. J., Haynes M. P., O'Donoghue A. A., Balonek T. J., 1998, *AJ*, 116, 2805
- Vassiliadis E., Wood P. R., 1993, *ApJ*, 413, 641
- Vassiliadis E., Wood P. R., 1994, *ApJS*, 92, 125
- Ventura P., D'Antona F., 2005, *A&A*, 431, 279
- Ventura P., Stanghellini L., Dell'Agli F., García-Hernández D. A., 2012, *MNRAS*, 452, 3395
- Wachlin F. C., Miller Bertolami M. M., Althaus L. G., 2011, *A&A*, 533, A139
- Wachter A., Winters J. M., Schröder K.-P., Sedlmayr E., 2008, *A&A*, 486, 497
- Weiss A., Ferguson J. W., 2009, *A&A*, 508, 1343

This paper has been typeset from a $\text{\TeX}/\text{\LaTeX}$ file prepared by the author.